THESIS APPROVAL

GRADUATE SCHOOL, KASETSART UNIVERSITY

Master of Engineering (Mechanical Engineering)

DEGREE

Mechanical Engineering | Mechanical Engineering

FIELD | **DEPARTMENT**

TITLE: An Evaluation of Existing Antegrade and Retrograde Humeral Nail in the Thai Humerus

NAME: Mr. Pongnarin Jeamwatthanachai

THIS THESIS HAS BEEN ACCEPTED BY

..... **THESIS ADVISOR**

(Assistant Professor Supasit Rodkwan, Ph.D.)

..... **THESIS CO-ADVISOR**

(Professor Banchong Mahaisavariya, M.D.)

..... **THESIS CO-ADVISOR**

(Mr. Kriskrai Sitthiseripratip, D.Eng.)

..... **DEPARTMENT HEAD**

(Associate Professor Chawalit Kittichaikarn, Ph.D.)

APPROVED BY THE GRADUATE SCHOOL ON .....

..... **DEAN**

(Associate Professor Gunjana Theeragool, D.Agr.)

THESIS

AN EVALUATION OF EXISTNG ANTEGRADE AND RETROGRADE HUMERAL NAIL IN THE THAI HUMERUS

PONGNARIN JEAMWATTHANACHAI

A Thesis Submitted in Partial Fulfillment of
the Requirements for the Degree of
Master of Engineering (Mechanical Engineering)
Graduate School, Kasetsart University
2009

Pongnarin Jeamwatthanachai 2009: An Evaluation of Existing Antegrade and Retrograde Humeral Nail in the Thai Humerus. Master of Engineering (Mechanical Engineering), Major Field: Mechanical Engineering, Department of Mechanical Engineering. Thesis Advisor: Assistant Professor Supasit Rodkwan, Ph.D. 104 pages.

This study presents the virtual simulation method to evaluate geometric mismatch of the standard humeral nail and biomechanical study of intramedullary nailing of the humeral shaft fracture using finite element method. In geometric mismatch study, the analysis was performed with nail inserted in the seventy-six cadaveric Thai humeri. The region was considered at 50-mm from the proximal to the distal part with 10-mm interval using two techniques; antegrade and retrograde insertion. The results showed 1) the diameter of the medullary canal averaged 7.85-13.78 mm, 2) the minimal reaming diameter to accommodate the nail insertion virtually averaged 8.84-14.83 mm for antegrade approach and 8.77-29.26 mm for retrograde approach.

A finite element method was employed to analyze the bone having the fracture gap on the humeral shaft with the humeral nail at normal and severe abduction using antegrade and retrograde approaches. The muscle forces of rotator cuff and deltoid were applied in loading conditions. Although the analysis showed that the intramedullary nail of retrograde nailing produced the von Mises stress on the nail slightly higher than antegrade nailing, the retrograde approach gave better results in biomechanical stability. Therefore the retrograde technique was preferred than antegrade technique. In addition, for the post operative of humeral shaft fracture, the patient should hang their arm in zero degree abduction or natural position and the ninety degree abduction should be avoided.

..../...../.....

Student's signature Thesis Advisor's signature

ACKNOWLEDGEMENTS

I would like to grateful thank and deeply indebted to my thesis advisor, Asst. Prof. Dr. Supasit Rodkwan for guidance, encouragement and valuable advice for completely writing of thesis. I would sincerely like to thank Prof. Banchong Mahaisavariya, Dr. Kriskrai Sitthiserripratip, my committees, and also Asst. Prof. Dr. Peerayot Sanposh and Assoc. Prof. Dr. Chaosuan Kanchanomai from Graduate School for their valuable comments and suggestion.

I would like to thank my friends at the Medical rapid prototyping laboratory, National Metal and Materials Technology Center (MTEC), and Mr. Panya Aroonjarattham for their assistance. I would also like to thank the Department of Anatomy, Faculty of Medicine Siriraj Hospital, Mahidol University for their kind support of providing cadaveric humeri specimens, and the National Metal and Materials Technology Center (MTEC), Thailand for their kind support of providing the use of their facilities. I would like to thank Thailand Graduate Institute of Science and Technology (TGIST) for the scholarship.

Finally, I am especially appreciated my parents, my brother and my friends for their continuing encouragements and support.

Pongnarin Jeamwatthanachai

January 2009

TABLE OF CONTENTS

LIST OF TABLES

LIST OF FIGURES

LIST OF FIGURES (Continued)

LIST OF FIGURES (Continued)

LIST OF FIGURES (Continued)

LIST OF FIGURES (Continued)

LIST OF ABBREVIATIONS

U	=	Displacement
R	=	Load vector
${}^{t}R$	=	External applied nodal point force
${}^{t}F$	=	Nodal point force
S	=	Shape function
u	=	Nodal displacement
v	=	Nodal displacement
w	=	Nodal displacement
V	=	Volume of tetrahedral element
$\vec{\delta}$	=	Displacement vector
σ_{xx}	=	Normal stress along x-axis
σ_{yy}	=	Normal stress along y-axis
σ_{zz}	=	Normal stress along z-axis
τ_{xy}	=	Shear stress in the x-y plane
τ_{yz}	=	Shear stress in the y-z plane
τ_{xz}	=	Shear stress in the x-z plane
ε_{xx}	=	Normal strain along x-axis
ε_{yy}	=	Normal strain along y-axis
ε_{zz}	=	Normal strain along z-axis
γ_{xy}	=	Shear strain in x-y plane
γ_{yz}	=	Shear strain in y-z plane
γ_{xz}	=	Shear strain in x-z plane
E	=	Young's Modulus
ν	=	Poisson's Ratio
G	=	Shear Modulus
L	=	Linear differential operator

LIST OF ABBREVIATIONS (Continued)

Λ	=	Strain energy
A	=	Surface
P	=	Pressure
Tesla	=	Unit of magnetic flux density
MPa	=	Mega Pascal (unit)
mm	=	millimeter (unit)
$\hat{i}$	=	Unit vector along x-axis
$\hat{j}$	=	Unit vector along y-axis
$\vec{k}$	=	Unit vector along z-axis
2D	=	Two-dimensional
3D	=	Three-dimensional
N	=	Newton
CT	=	Computerized Tomography
MRI	=	Magnetic Resonance Imaging
FEA	=	Finite Element Analysis
CAD	=	Computer Aided Design

AN EVALUATION OF EXISTING ANTEGRADE AND RETROGRADE HUMERAL NAIL IN THE THAI HUMERUS

INTRODUCTION

1. Background

The humeral fractures have been variously treated ranging from conservative to operative methods, the latter including open reduction and internal fixation with plate and screws, tension band wiring, intramedullary devices and prosthetic replacement. The intramedullary fixation device is accepted as treatment for minimal invasive technique with low morbidity, providing simultaneously rapid recovery and prompt return to work and everyday life activities. Intramedullary fixation of long bones has been increasingly preferred especially following traumatic injuries and pathologic fractures (Blum *et al*., 2001).

(A) (B) (C)

Figure 1 Three operative methods of humeral shaft fracture fixation : (A) Splint, (B) plate and screw and (C) intramedullary nail.

Source: http://www.wheelessonline.com (2009).

To preserve the biological tissue, minimal invasive becomes a new trend to treat the bone fracture. The intramedullary fixation is considered a treatment for minimal invasive technique with low morbidity, providing simultaneously rapid recovery and prompt return to work and daily life activities. The humeral nail is an intramedullary device to be use for fracture stabilization in the shaft regions of the humerus.

2. Statement of the problem

At present most nails used in healing the fractures in Asian patients are imported from European or American country where the nail components are designed based on Caucasian database (Arunjarutthum *et al*., 2006). The use of un-proportionate nails may lead to complications in healing process such as weak bone, increase the risk of intraoperative and postoperative complications (Leung *et al*., 1996). Geometric mismatch studies on humerus revealed that there was some degree of mismatch and the geometric components of implant were not fit to the bone (Akpinar *et al*., 2003).

However, there is no report on the geometric mismatch of the standard humeral nail for the Asian humerus. The use of universal implants therefore presents some clinical complications in Asian patients. As a result, this work will focus on Asian humerus where morphometric study revealed that the dimensions of Asian proximal humerus were smaller and slightly different from those of Caucasian (Arunjarutthum *et al*., 2006). It is speculated that the standard humeral nail would display deviation from Asian humerus, and the given results would be applied for re-designing of the nail.

The insertion technique of the nail is one of factors influencing the clinical results. Literatures on insertion techniques on humeral fractures seem to suggest that antegrade insertion might be favorable or comparable to retrograde insertion, however, comparison of healing efficiency between both techniques have not been clearly demonstrated. A study on clinical performance of both techniques at humeral

shaft fracture with the new unreamed humeral nail (UHN) showed that retrograde insertion was technically more preferable than antegrade insertion (Blum *et al*., 2001).

In biomechanics term, the loads condition act on humerus differs from the femur. Humerus hangs by the muscle forces and the weight of arm is active at the distal bone, but the femoral load is active on the femoral head by body weight. There is a few report on humeral biomechanics (Van der Helm and Veenbaas, 1991, Wuelker *et al*., 1995, and Kedgley *et al*., 2007). One study used the cadaveric model to determine the abduction angle and muscle forces magnitude but not include the direction of muscle forces (Debski *et al*., 1995). This study will use the advance techniques to examine the direction and magnitude of muscle forces that active in normal abduction condition. The FEA is used to verify the stress distribution on the standard humeral nail when inserted in the Thai humerus.

3. Objective

3.1 To investigate the geometric mismatch of standard humeral nail in the Asian humerus using the antegrade and retrograde insertion techniques.

3.2 To study the stress/strain distribution in humeral nail and Humerus under physiological-like loading conditions.

4. Scope of the study

4.1 The geometrical assessment results based on the cadaveric dry bone, which may be slightly different from the living bone tissue.

4.2 The muscle loading during abduction were taken from the mechanical testing to evaluate mechanical performance by means of a finite element method.

LITERATURE REVIEW

1. Anatomy of humerus

The humerus is a long bone in the arm or forelimb that runs from the shoulder to the elbow as shown in Figure 2 and 3. Anatomically, it connects the scapula and the ulna, and consists of the following three sections.

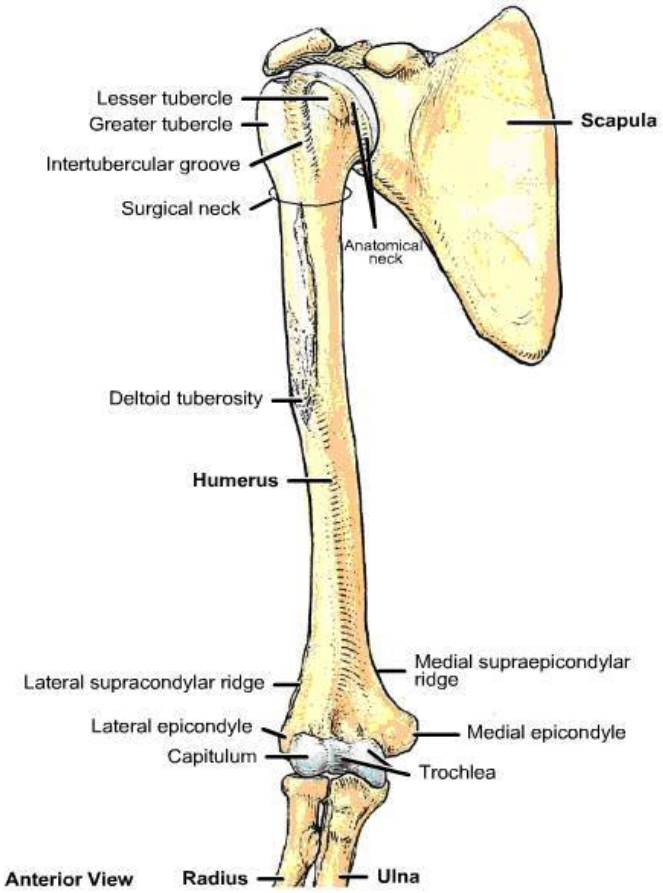

Figure 2 Humerus (Anterior view).

Source: Dynamic Human Anatomy 2.0 software (2005).

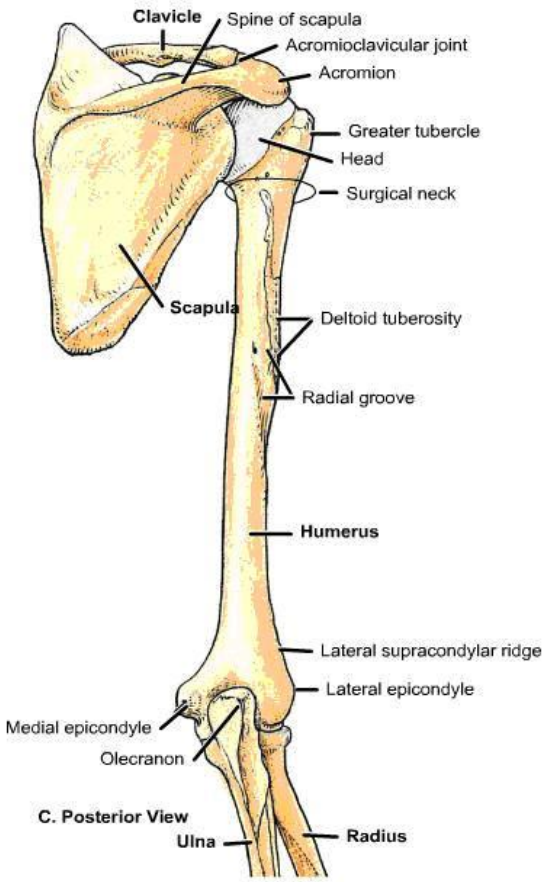

Figure 3 Humerus (Posterior view).

Source: Dynamic Human Anatomy 2.0 software (2005).

1.1 Upper extremity of humerus

The upper extremity of the humerus (proximal humerus) consists of a large rounded *head* joined to the body by a constricted portion called the neck, and two eminences, the greater and lesser tubercles.

1.1.1 The humeral head

The humeral head, nearly hemispherical in form. It is directed upward, medialward, and a little backward, and articulates with the glenoid cavity of the scapula. The circumference of its articular surface is slightly constricted and is

termed the anatomical neck, in contradistinction to a constriction below the tubercles called the surgical neck which is frequently the seat of fracture.

1.1.2 The anatomical neck

The Anatomical Neck is obliquely directed, forming an obtuse angle with the body. It is best marked in the lower half of its circumference; in the upper half it is represented by a narrow groove separating the head from the tubercles. It affords attachment to the articular capsule of the shoulder-joint, and is perforated by numerous vascular foramina. Fracture of the anatomical neck rarely occurs. The anatomical neck of the humerus is an indentation distal to the head of the humerus on which the articular capsule attaches.

1.1.3 The greater tubercle

The greater tubercle is situated lateral to the head and lesser tubercle, and just lateral to the anatomical neck. Its upper surface is rounded and marked by three flat impressions: the highest of these gives insertion to the supraspinatus muscle; the middle to the infraspinatus muscle; the lowest one, and the body of the bone for about 2.5 cm. below it, to the teres minor muscle. The lateral surface of the greater tubercle is convex, rough, and continuous with the lateral surface of the body. The lesser tuberosity or The lesser tubercle, is although smaller,it's more prominent than the greater: it is situated in front, and is directed medialward and forward. Above and in front it presents an impression for the insertion of the tendon of the subscapularis muscle.

1.1.4 The intertubercular (bicipital) groove

The tubercles are separated from each other by a deep groove, the intertubercular groove (bicipital groove), which lodges the long tendon of the biceps brachii muscle and transmits a branch of the anterior humeral circumflex artery to the shoulder-joint. It runs obliquely downward, and ends near the junction of the

upper with the middle third of the bone. In the fresh state its upper part is covered with a thin layer of cartilage, lined by a prolongation of the synovial membrane of the shoulder-joint; its lower portion gives insertion to the tendon of the latissimus dorsi muscle. It is deep and narrow above, and becomes shallow and a little broader as it descends. Its lips are called, respectively, the crests of the greater and lesser tubercles (bicipital ridges), and form the upper parts of the anterior and medial borders of the body of the bone.

1.1.5 The surgical neck

The surgical neck is a narrow area distal to the tubercles that is a common site of fracture. It makes contact with the axillary nerve and the posterior humeral circumflex artery.

1.2 Body of humerus

The body or shaft of the humerus is almost cylindrical in the upper half of its extent, prismatic and flattened below, and has three borders and three surfaces.

1.2.1 Anterior borders

The anterior border runs from the front of the greater tubercle above to the coronoid fossa below, separating the antero-medial from the antero-lateral surface. Its upper part is a prominent ridge, the crest of the greater tubercle; it serves for the insertion of the tendon of the pectoralis major muscle. About its center it forms the anterior boundary of the deltoid tuberosity, on which the deltoid muscle attaches; below, it is smooth and rounded, affording attachment to the brachialis muscle.

1.2.2 Lateral borders

The lateral border runs from the back part of the greater tubercle to the lateral epicondyle, and separates the anterolateral from the posterior surface. Its upper half is rounded and indistinctly marked, serving for the attachment of the lower part of the insertion of the teres minor muscle, and below this giving origin to the lateral head of the triceps brachii muscle; its center is traversed by a broad but shallow oblique depression, the spiral groove (musculospiral groove). The radial nerve runs in the spiral groove. Its lower part forms a prominent, rough margin, a little curved from behind forward, the lateral supracondylar ridge, which presents an anterior lip for the origin of the brachioradialis muscle above, and extensor carpi radialis longus muscle below, a posterior lip for the triceps brachii muscle, and an intermediate ridge for the attachment of the lateral intermuscular septum.

1.2.3 Medial borders

The medial border extends from the lesser tubercle to the medial epicondyle. Its upper third consists of a prominent ridge, the crest of the lesser tubercle, which gives insertion to the tendon of the teres major muscle. About its center is a slight impression for the insertion of the coracobrachialis muscle, and just below this is the entrance of the nutrient canal, directed downward; sometimes there is a second nutrient canal at the commencement of the radial sulcus. The inferior third of this border is raised into a slight ridge, the medial supracondylar ridge, which becomes very prominent below; it presents an anterior lip for the origins of the brachialis muscle and the pronator teres muscle, a posterior lip for the medial head of the triceps brachii muscle, and an intermediate ridge for the attachment of the medial intermuscular septum.

1.2.4 Antero-lateral surface

The antero-lateral surface is directed lateralward above, where it is smooth, rounded, and covered by the deltoid muscle; forward and lateralward below, where it is slightly concave from above downward, and gives origin to part of the brachialis. About the middle of this surface is a rough, triangular elevation, the deltoid tuberosity for the insertion of the deltoid muscle; below this is the radial sulcus, directed obliquely from behind, forward, and downward, and transmitting the radial nerve and profunda artery. The antero-medial surface, less extensive than the antero-lateral, is directed medialward above, forward and medialward below; its upper part is narrow, and forms the floor of the intertubercular groove which gives insertion to the tendon of the latissimus dorsi muscle; its middle part is slightly rough for the attachment of some of the fibers of the tendon of insertion of the coracobrachialis muscle; its lower part is smooth, concave from above downward, and gives origin to the brachialis muscle.

1.2.5 Posterior surface

The posterior surface appears somewhat twisted, so that its upper part is directed a little medialward, its lower part backward and a little lateralward. Nearly the whole of this surface is covered by the lateral and medial heads of the Triceps brachii, the former arising above, the latter below the radial sulcus.

1.3 Lower extremity of humerus

The lower extremity of the humerus is flattened from before backward and curved slightly forward; it ends below in a broad, articular surface, which is divided into two parts by a slight ridge.

1.3.1 Articular surface

The articular surface extends a little lower than the epicondyles, and is curved slightly forward; its medial extremity occupies a lower level than the lateral. The lateral portion of this surface consists of a smooth, rounded eminence, named the capitulum of the humerus; it articulates with the cupshaped depression on the head of the radius, and is limited to the front and lower part of the bone. On the medial side of this eminence is a shallow groove, in which is received the medial margin of the head of the radius. Above the front part of the capitulum is a slight depression, the radial fossa, which receives the anterior border of the head of the radius, when the forearm is flexed.

1.3.2 Borders

The medial portion of the articular surface is named the trochlea, and presents a deep depression between two well-marked borders; it is convex from before backward, concave from side to side, and occupies the anterior, lower, and posterior parts of the extremity.

a) The lateral border separates it from the groove which articulates with the margin of the head of the radius.

b) The medial border is thicker, of greater length, and consequently more prominent, than the lateral.

The grooved portion of the articular surface fits accurately within the semilunar notch of the ulna; it is broader and deeper on the posterior than on the anterior aspect of the bone, and is inclined obliquely downward and forward toward the medial side.

1.3.3 Fossae

Above the front part of the trochlea is a small depression, the coronoid fossa, which receives the coronoid process of the ulna during flexion of the forearm. Above the back part of the trochlea is a deep triangular depression, the olecranon fossa, in which the summit of the olecranon is received in extension of the forearm. These fossæ are separated from one another by a thin, transparent lamina of bone, which is sometimes perforated by a supratrochlear foramen; they are lined in the fresh state by the synovial membrane of the elbow-joint, and their margins afford attachment to the anterior and posterior ligaments of this articulation.

1.3.4 Condyles

a) The lateral epicondyle is a small, tuberculated eminence, curved a little forward, and giving attachment to the radial collateral ligament of the elbow-joint, and to a tendon common to the origin of the Supinator and some of the Extensor muscles.

b) The medial epicondyle, larger and more prominent than the lateral, is directed a little backward; it gives attachment to the ulnar collateral ligament of the elbow-joint, to the pronator teres, and to a common tendon of origin of some of the Flexor muscles of the forearm; the ulnar nerve runs in a groove on the back of this epicondyle.

2. Muscle around shoulder joint

The shoulder joint is a ball-and-socket joint that consists of the round head of the humerus and the shallow glenoid cavity of the scapula. The joint capsule of the shoulder is attached along the circumference of the glenoid cavity and the anatomical neck of the humerus. Although it completely envelopes the joint, the capsule is very loose, and by itself is unable to keep the bones of the joint in close contact. However,

muscles and tendons surround and reinforce the capsule, keeping together the articulating parts of the shoulder.

2.1 Muscles move the arm

The arm is one of the more freely movable parts of the body because muscles connect the humerus to regions of the pectoral girdle, ribs, and vertebral column as shown in Figure 4. These muscles can be grouped according to their primary actions-flexion, extension, abduction, and rotation as shown in Figure 5.

Flexors	**Abductors**	**Extensors**	**Rotators**
Coracobrachialis	Supraspinatus	Teres major	Subscapularis
Pectoralis major	Deltoid	Latissimusdorsi	Infraspinatus
			Teres minor

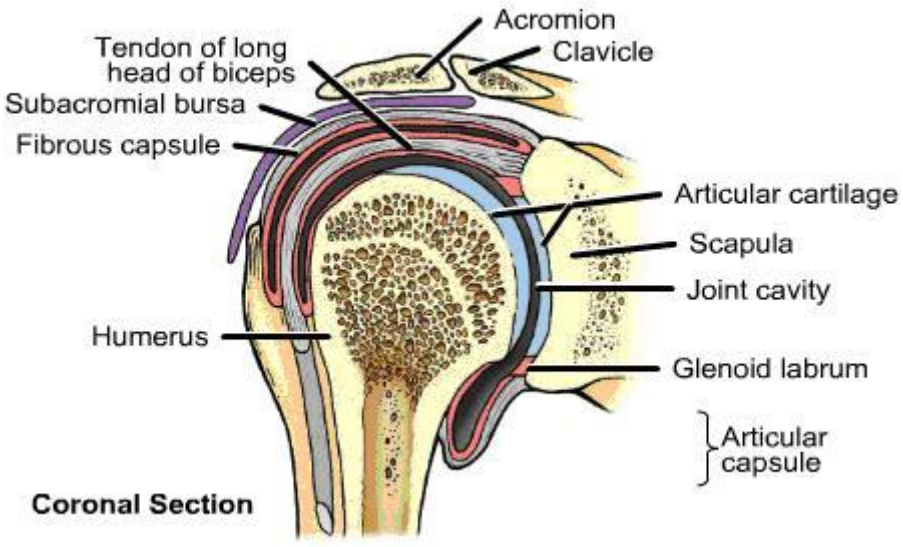

Figure 4 Cross sectional of shoulder joint.

Source: Dynamic Human Anatomy 2.0 software (2005).

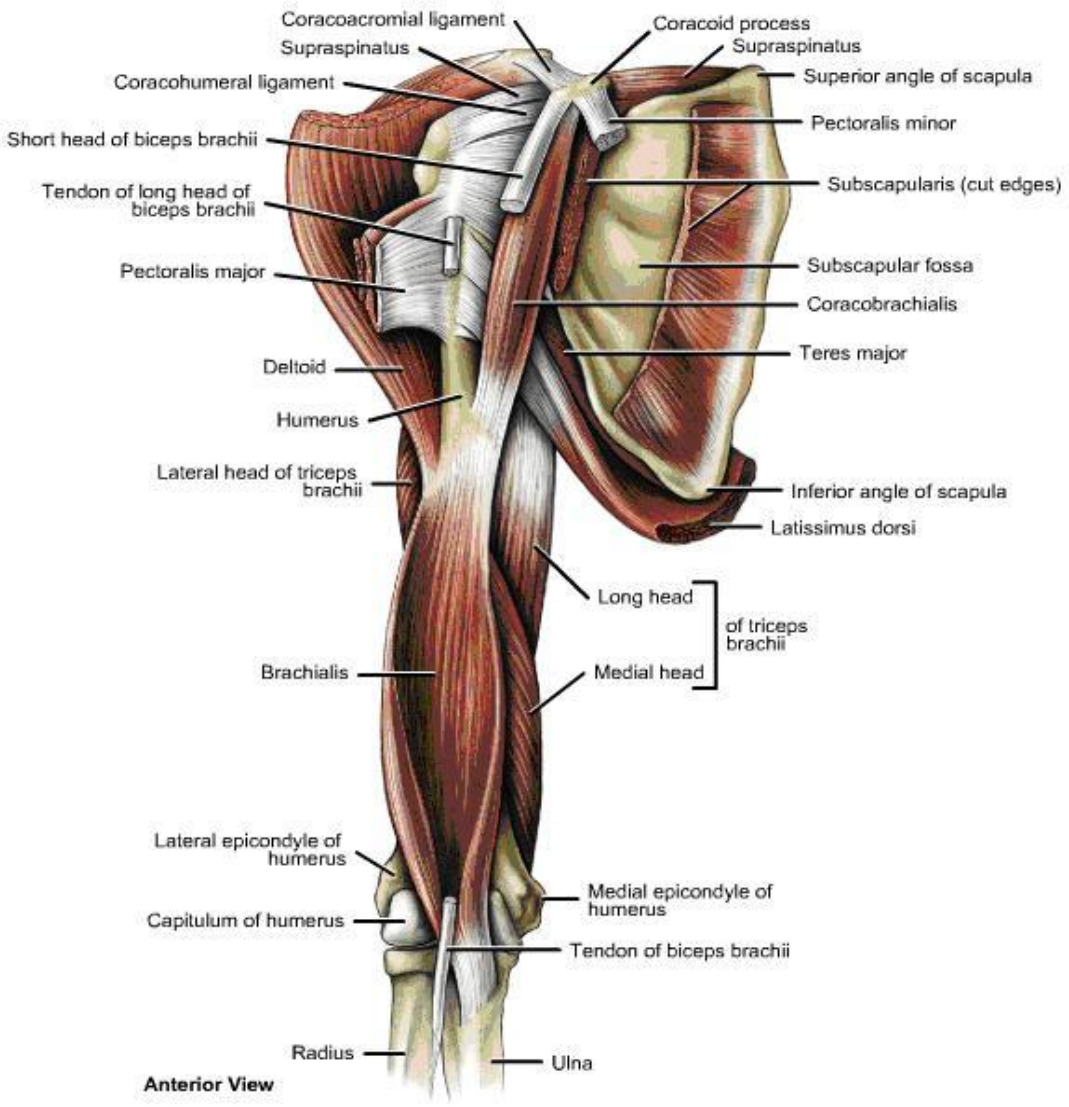

Figure 5 Muscles around the humerus.

Source: Dynamic Human Anatomy 2.0 software (2005).

2.1.1 The coracobrachialis extends from the scapula to the middle of the humerus along its medial surface. It flexes and adducts the arm.

2.1.2 The pectoralis major is a thick, fan-shaped muscle located in the upper chest. Its fibers extend from the center of the thorax through the armpit to the humerus. This muscle primarily pulls the arm forward and across the chest. It can also rotate the humerus medially and adduct the arm from a raised position.

2.1.3 The supraspinatus is located in the depression above the spine of the scapula on its posterior surface. It connects the scapula to the greater tubercle of the humerus and abducts the arm.

2.1.4 The deltoid is a thick, triangular muscle that covers the shoulder joint. It connects the clavicle and scapula to the lateral side of the humerus and abducts the arm. The deltoid's posterior fibers can extend the humerus, and its anterior fibers can flex the humerus.

2.1.5 The teres major connects the scapula to the humerus. It extends the humerus and can also adduct and rotate the arm medially.

2.1.6 The latissimus dorsi is a wide, triangular muscle that curves upward from the lower back, around the side, and to the armpit. It can extend and adduct the arm and rotate the humerus medially. It also pulls the shoulder downward and back. This muscle is used to pull the arm back in swimming, climbing, and rowing.

2.1.7 The subscapularis is a large, triangular muscle that covers the anterior surface of scapula. It connects the scapula to the humerus and rotates the arm medially.

2.1.8 The infraspinatus occupies the depression below the spine of the scapula on its posterior surface. The fibers of this muscle attach the scapula to the humerus and rotate the arm laterally.

2.1.9 The teres minor is a small muscle connecting the scapula to the humerus. It rotates the arm laterally.

3. Fractures of humerus

3.1 Fracture classification

The classification of humeral shaft fractures based on the nature and location of the primary fracture line, an estimation of the kinematics of the injury, and associated soft tissue trauma.

3.1.1 Fracture personality (direction and character of the fracture)

3.1.1.1 Transverse fractures that are not internally splinted by the intravascular septa may be difficult to control.

3.1.1.2 Oblique fractures usually unite without difficulty.

3.1.1.3 Spiral fractures in the distal third may produce a radial nerve injury and it segmental injuries are also difficult to control.

3.1.1.4 Comminuted fractures are associated with soft tissue injury and difficult to manage by internal fixation, but unite well with nonopertive fracture management.

3.1.2 Associated soft tissue injury

3.1.2.1 Open: Grade1 (low energy, wound less than 1 cm), Grade2 (moderate energy and soft tissue damage, wound greater than 1 cm) and Grade3 (high energy, wound greater than 10 cm)

3.1.2.2 Periarticular injury: Glenohumeral, Elbow joint

3.1.2.3 Nerve injury: Radial nerve, Median nerve, Ulnar nerve

3.1.2.4 Vascular injury: Brachial artery, Brachial vein

3.2 Humeral fracture

3.2.1 Proximal humeral fractures occur near the shoulder joint as shown in Figure 6. The shoulder joint is a ball-and-socket joint, with the ball being the top of the humerus bone. Fractures of this ball are considered proximal humerus fractures. These fractures may involve the insertion of the important rotator cuff tendons. Because these tendons are important to shoulder motion, treatment may depend on the position of these tendon insertions.

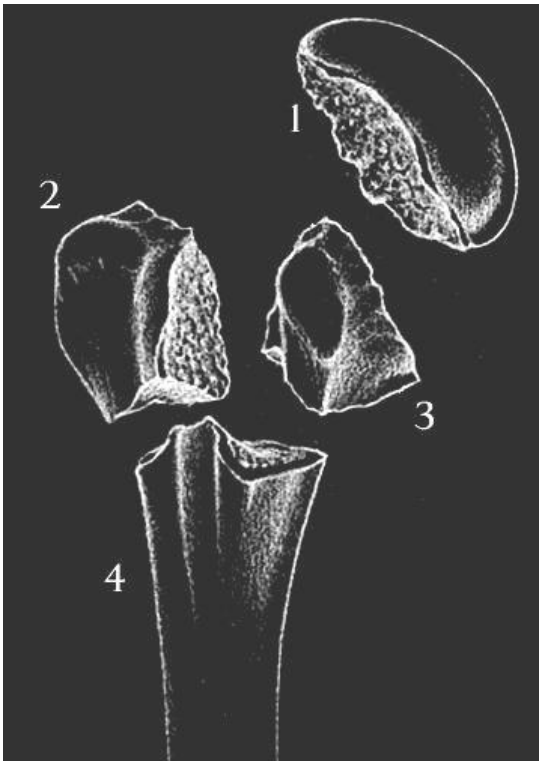

Figure 6 The Neer classification of the proximal humerus fracture, the proximal humerus is made up of four parts: 1) Humeral head, 2) Greater tubercle, 3) Lesser tubercle and 4) Diaphysis (shaft).

Source: Neer (2006).

3.2.2 Mid-shaft humeral fractures occur away from the shoulder and elbow joints as shown in Figure 7. Most humeral shaft fractures will heal without surgery, but there are some situations that require surgical intervention. These injuries are commonly associated with injury to one of the large nerves in the arm, called the radial nerve. Injury to this nerve may cause symptoms in the wrist and hand.

Figure 7 Mid-shaft fracture of humerus.
Source: http://www.wheelessonline.com (2009).

3.2.3 Distal humeral fractures are uncommon injuries in adults. These fractures occur near the elbow joint as shown in Figure 8. These fractures most often require surgical treatment unless the bones are held in proper position. This type of fracture is much more common in children, but the treatment is very different in this age group.

Figure 8 Distal fracture of humerus.
Source: http://www.wheelessonline.com (2009).

3.3 Fracture management

3.3.1 Non-operative treatment

Most humeral shaft fractures can be managed non-operatively with expected union rates approaching 100%. The generally good outcomes with non-operative treatment may be due in part, to tolerance of malunion in the arm. Functional fracture bracing has largely replaced all other procedures as the treatment of choice for these injuries.

a) Hanging arm casts
b) Velpeau dressing/sling and swathe
c) Coaptation splint
d) Abduction Splint-Shoulder Spica Cast
e) Skeletal Traction
f) Functional Bracing

3.3.2 Operative treatment

Given the relative propensity for delayed union in transverse or short oblique fractures managed nonoperatively in an active individual, these fracture patterns may be relative indications for surgery. Alternatives to operative stabilization include intramedullary nailing, compression plating and screw osteosynthesis, and external fixation.

a) Plate osteosynthesis
b) Intramedullary nailing

4. Material properties of bone

4.1 Cortical bone

The mechanical properties of bone tissue are typically determined by measuring the deformation of small, uniform specimens during application of simple, well-defined loads. Figure 9 illustrates a typical test that involves subjecting a machined cortical bone specimen to tensile loads. Dumbbell-shaped tensile specimens are typically used, so that failure occurs in a reproducible location.

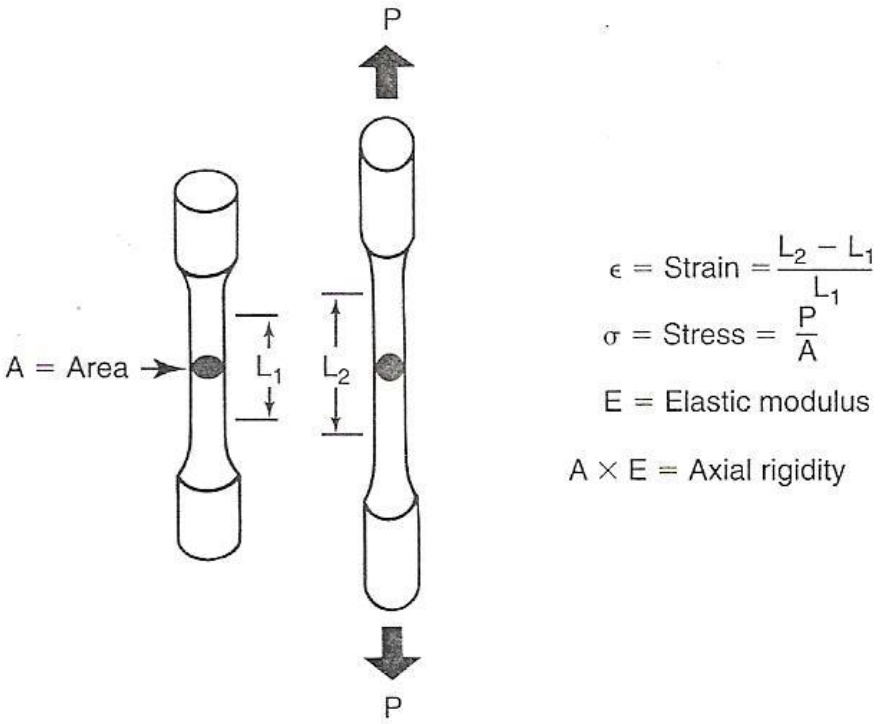

Figure 9 Simple uniaxial tensile test with a dumbbell-shaped specimen, P is the applied load and $(L_2\text{-}L_1)/L_1$ is the strain between two points along the specimen's axis.

Source: Browner *et al*. (1998).

Two parameters are monitored during the tensile test: the applied force and the displacement between two points along the long axis of the specimen. The resulting force displacement curve provides an indication of the stiffness and failure load of the bone specimen, but the data are useful only for specimens with the same geometry as the one tested. To provide material property data that can be applied to any specimen geometry, the force and displacement data are converted to stress and strain. This is a normalization process that eliminates the influence of specimen geometry. The stress in the bone specimen is calculated as the applied force divided by the cross-sectional area, and the strain is measured as the percentage change in length of a defined length of the specimen. A typical stress-strain curve for a tensile test of cortical bone is shown in Figure 10.

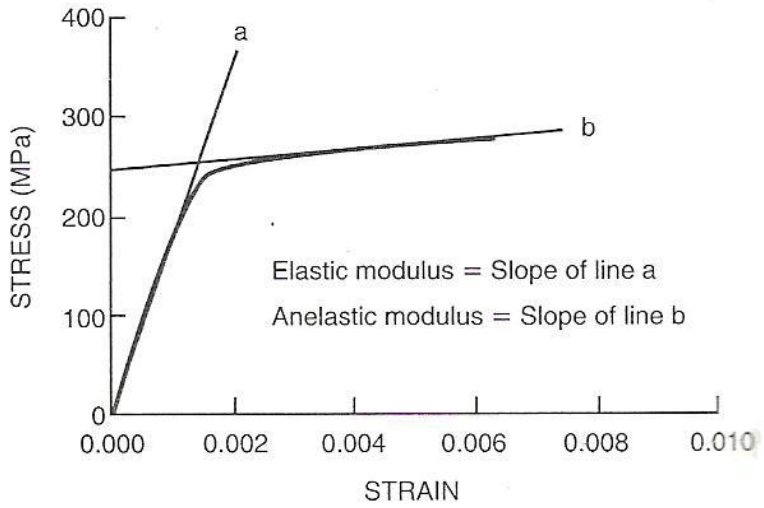

Figure 10 Typical stress-strain curve for human cortical bone showing the curve regions where the elastic and anelastic moduli are calculated.

Source: Browner *et al*. (1998).

The elastic modulus of bone tissue or structural materials such as stainless steel, titanium, or polymethyl methacrylate is determined from the slope of the initial, linear part of the curve. The point at which the slope of the stress-strain curve decreases is the yield point of the bone, and the maximal recorded stress is the ultimate strength of the tissue. After the bone has yield, the slope of the stress-strain curve drops to a new value termed the anelastic modulus. The area under the stress-strain curve reflects the capacity of bone to absorb energy. The capacity to absorb energy increases with yield strength, but the greatest energy absorption is typically seen for bones with high ultimate strains, where substantial energy is absorbed during post yield deformation.

Bone is loaded cyclically during many activities of daily living, and the load required to cause bone to fail will be dramatically lower if that load is applied repeatedly. The number of cycles of stress that bone can tolerate decreases as the stress level increases. This property of bone is measured using stress-versus-number of cycles to failure (SN) curves. These curves depend on the type of loading (axial,

bending, or torsion), the loading rate, and the physical composition of the bone. The mechanisms in bone that determine its behavior under cyclical loading are beginning to be understood.

The stress-strain behavior of cortical bone is also strongly dependent on the orientation of bone microstructure with respect to the loading direction. Several investigators have shown that cortical bone is both stronger and stiffer in the longitudinal direction than in the transverse direction. Materials such as bone whose mechanical properties depend on the loading direction are said to be anisotropic.

4.2 Trabecular bone

The major physical difference between trabecular bone and cortical bone is the increased porosity exhibited by trabecular bone. This porosity is reflected by measurements of the apparent density. In the human skeleton, the apparent density of trabecular bone ranges from approximately 0.1 g/cm^3 to 1.0 g/cm^3, whereas the apparent density of cortical bone is about 1.8 g/cm^3. A trabecular bone specimen with an apparent density of 0.2 g/cm^3 has a porosity of about 90%.

The compressive stress-strain properties of trabecular bone are markedly different from those of cortical bone and are similar to the compressive behavior of many porous engineering materials that absorb energy on impact. Stress-strain curves for trabecular bone in compression exhibit an initial elastic region followed by yield as shown in Figure 11. The slope of the initial elastic region ranges from one to two orders of magnitude less than that of cortical bone. Yield is followed by a long plateau region created as more trabeculae fracture. The fractured trabeculae begin to fill the marrow spaces at approximately 50% strain. Further loading of the specimen after the pores are filled is associated with a marked increase in specimen modulus.

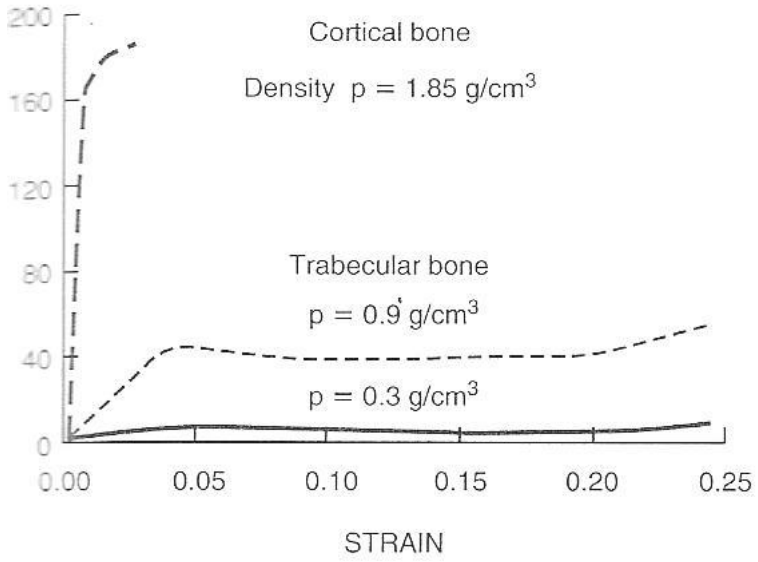

Figure 11 Compressive stress-strain curves for cortical and trabecular bone of different densities.

Source: Browner *et al*. (1998).

5. Bone repair and fracture healing

The process of bone healing follows an ordered progression based on the material properties of the healing constituents. The tissues associated with healing are able to withstand a determined degree of internal motion or strain depending up on the tissue type. Granulation tissue is able to withstand 100% strain (it can increase length in 100%), cartilage 15% strain and bone 2% strain as shown in Figure 12(B) (Cross). Therefore cartilage, for example, will not form in the healing process until fibrous tissue has stabilized the fracture fragments to within 15% strain. Tissue is more effective at reducing strain the further it is from the center of the bone as shown in Figure 12(C), hence the large callus is seen with unstable fractures. By stabilizing fractures to varying degree, we can skip or shorten the time required to reach a strain environment in which a given tissue can form. In the most stable repairs, we can skip all intermediate tissue types and progress to direct bone formation. The all process was shown in Figure 12.

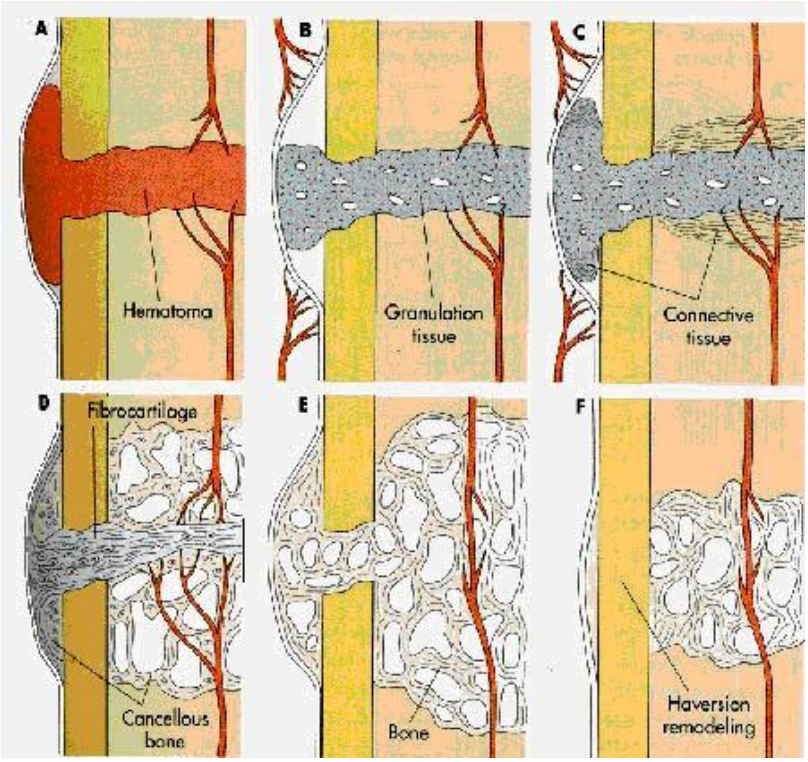

Figure 12 The processes of bone repair and fracture healing: A) Hematoma, B) Granulation tissue, C) Connective tissue, D) Cancellous bone, E) Bone and F) Haversion remodeling.

Source: College of Veterinary Medicine (2000).

There are two types of fracture healing: secondary bone healing and primary bone healing.

6. Secondary bone healing (with callus formation)

The type of union that occurs with spontaneous fracture healing and forms of immobilization or fixation that do not provide rigid stabilization of a fracture is called a secondary bone healing. This type of fracture healing occurs in three distinct but overlapping stages: 1) the early inflammatory stage; 2) the repair stage; and 3) the late remodeling stage (DePalma *et al*., 1972, Burchardt and Enneking, 1978, and Kalfas, 2001).

In the inflammatory stage, a hematoma develops within the fracture site during the first few hours and days. Inflammatory cells (macrophages, monocytes, lymphocytes, and polymorphonuclear cells) and fibroblasts infiltrate the bone under prostaglandin mediation. This results in the formation of granulation tissue, ingrowth of vascular tissue, and migration of mesenchymal cells. The primary nutrient and oxygen supply of this early process is provided by the exposed cancellous bone and muscle.

During the repair stage, fibroblasts begin to lay down a stroma that helps support vascular ingrowth. It is during this stage that the presence of nicotine in the system can inhibit this capillary ingrowth (Rubenstein *et al*., 1991, Daftari *et al*., 1994, Riebel *et al*., 1995, and Silcox *et al.* 1995). A significantly decreased union rate had been consistently demonstrated in tobacco abusers (Brown *et al*., 1986, Blumenthal *et al*., 1988, and Bishop *et al*., 1996). As vascular ingrowth progresses, a collagen matrix is laid down while osteoid is secreted and subsequently mineralized, which leads to the formation of a soft callus around the repair site. In terms of resistance to movement, this callus is very weak in the first 4 to 6 weeks of the healing process and requires adequate protection in the form of bracing or internal fixation. Eventually, the callus ossifies, forming a bridge of woven bone between the fracture fragments. Alternatively, if proper immobilization is not used, ossification of the callus may not occur, and an unstable fibrous union may develop instead.

Fracture healing is completed during the remodeling stage in which the healing bone is restored to its original shape, structure, and mechanical strength. Remodeling of the bone occurs slowly over months to years and is facilitated by mechanical stress placed on the bone. As the fracture site is exposed to an axial loading force, bone is generally laid down where it is needed and resorbed from where it is not needed. This is subjected to the Wolff's law (1892) of structural adaptation of bone, noting that bone placed under compressive or tensile stress is remodeled. Bone is formed where stresses require its presence and resorbed where stresses do not require it (Wolff, 1986 and Recker, 1992). Adequate strength is typically achieved in 3 to 6 months.

7. Primary bone healing (without callus formation)

Primary bone healing occurs with anatomic reduction and rigid (generally internal) fixation. As in secondary healing, there is interruption of the bone's blood supply and necrosis of the fracture ends. Remember this affects the cellular components (osteocytes) of the bone, but has little effect on the material components. There are two components to primary bone healing: gap healing and contact healing (Kalfas, 2001).

7.1 Gap healing

On a microscopic level (Kalfas, 2001), even a fracture that is perfectly reduced has irregular surfaces and this creates gaps between fragments. In the first stage of gap healing, gaps less than 200-500 microns (possibly up to 1000 microns) in width will be filled by direct bone formation. This means that neither connective tissue nor fibrocartilage preceded bone formation. In the second phase of gap healing, this disorganized woven bone is longitudinally reconstructed by Haversian remodeling. It should be stated that even with rigid internal fixation, gaps greater than l mm are partially filled with fibrous tissue, which is subsequently replaced by bone in a process similar to secondary bone healing.

7.2 Contact healing

Contact healing (Kalfas, 2001) occurs in areas where the fracture fragments are in direct apposition and results in union through direct ingrowth of Haversian systems across the fracture. Osteoclasts form cutting cones that advance across the fracture line forming a resorption cavity. This is followed by the growth of a capillary loop down the center of the resorption cavity. Mesenchymal cells and osteoprogenitor cells accompany these capillaries, become osteoblasts and produce osteoid closing cone. The conical shape of these bone forming units is accounted for by the relative speeds of the cutting and closing cones. The osteoclasts are

approximately 10 times faster than the osteoblasts and this has important implications on the timing of implant removal.

8. Biomechanics of fracture treatment

Many techniques are currently available for treatment of skeleton fracture, and many factors are important in choosing the best fixation. Each method of fixation imparts a specific level of stability to a fracture and thus directly influences fracture healing biology. When evaluating a fracture treatment method, the healing bone and the fracture treatment device should be considered as a mechanical system, with both the tissue and the device contributing to biomechanical behavior. The biomechanical behavior of the system can thus be altered by changes in tissue properties, changes to the fracture treatment device, or changes to the mechanical connection between device and tissue.

8.1 Internal fixation

8.1.1 Intramedullary Rods have several advantages in fracture treatment, including restoration of bony alignment and early recovery of weight bearing. The good clinical results and low rates of nonunion suggest that many current clinical applications of these devices provide a mechanical environment that facilitates fracture repair for selected fractures. Intramedullary rods are intended to stabilize a fracture by acting as an internal splint as shown in Figure 13, forming a composite structure in which both the bone and the rod contribute to fracture stability. This load-sharing property of rods is fundamental to their design and should be recognized when they are used for fracture treatment.

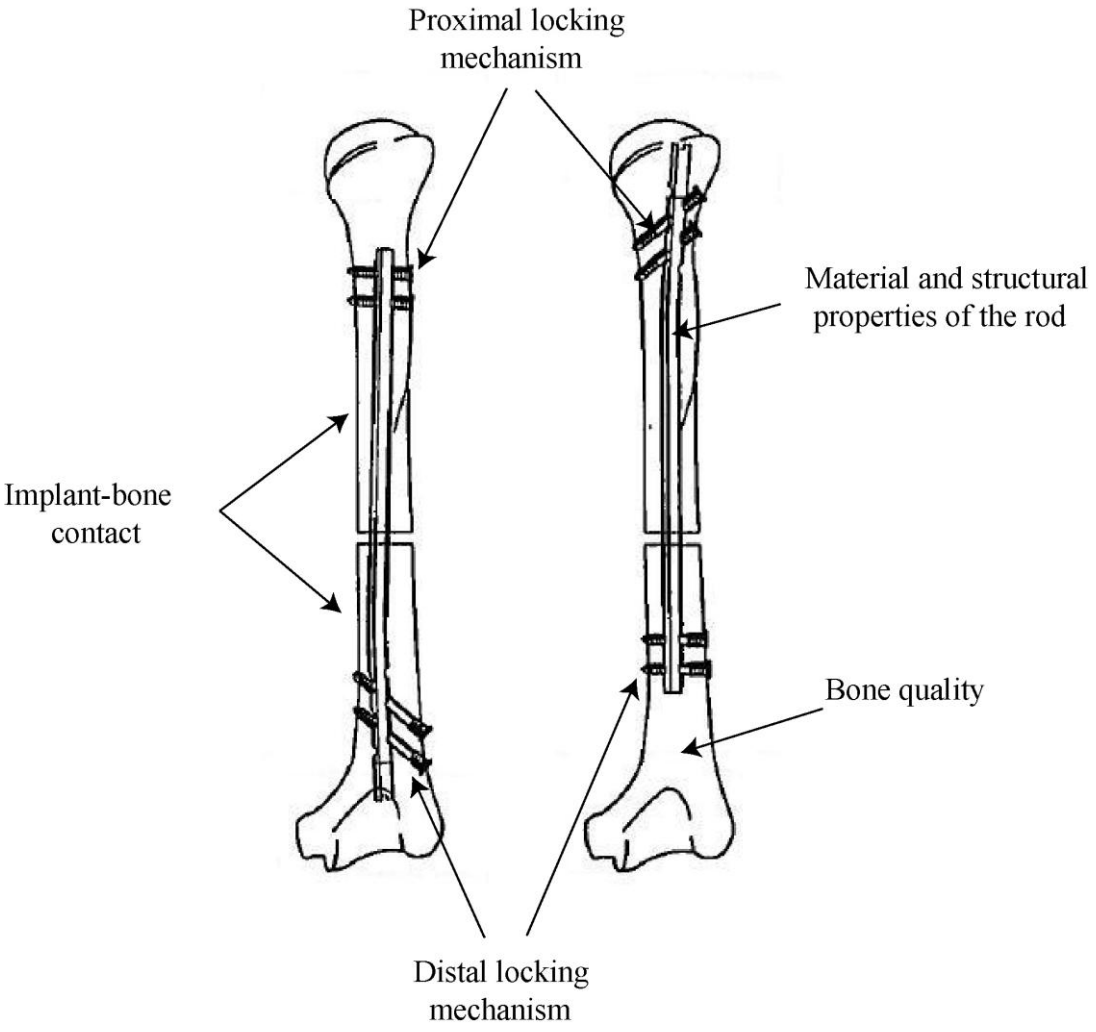

Figure 13 Factors important in intramedullary fracture fixation.
Source: Lin *et al*. (1998).

8.1.2 Bone Plate several basic biomechanical principals are important to fracture fixation using bone plates. Figure 14 illustrates some important parameters. It is crucial to realize that the plate and the bone together from a mechanical construct, with some load supported by the plate and some load passing between bone fragments. The interaction between plate and bone is also load-dependent; the plate may improve stability for one type of loading much more than for other types of loads.

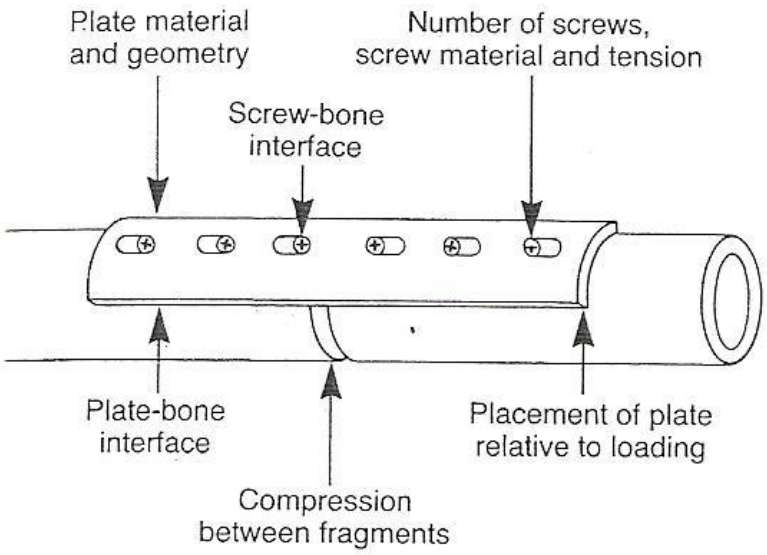

Figure 14 Factor affecting the stability of a plated fracture.
Source: Browner *et al*. (1998).

8.2 External fixation

Current external device provide a wide range of frame configuration and fracture stability option, making external fixation adaptable to many clinical situations. External fixation devices also provide convenient way to alter fixation rigidity during the course of healing and offer potential for monitoring the biomechanical progression of fracture healing. The stability provided by an external fixation device depends on both the frame configuration and the interaction between frame and bone fragments. As shown in Figure 15, several geometric, material and technical factors, as well as loading directions, can play a role in the biomechanics of external fixed fractures.

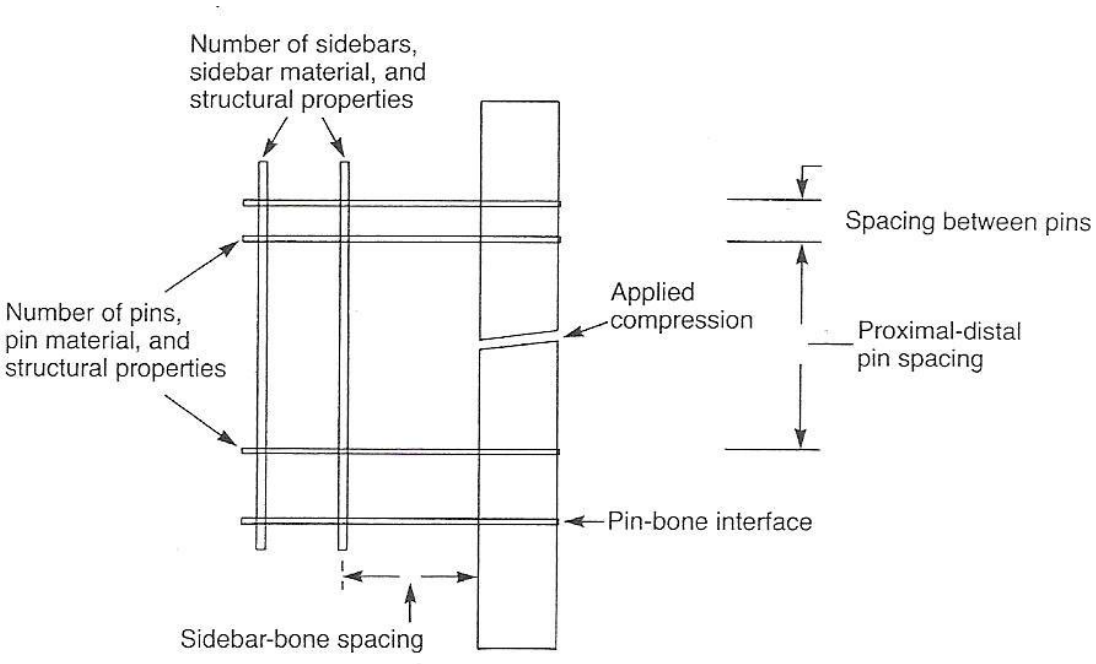

Figure 15 Factor affecting the stability of an externally fixed fracture.
Source: Browner *et al*. (1998).

9. Finite element analysis theorem

Bathe (1996), the finite element method is a numerical procedure for obtaining solution to many of the problems encountered in engineering analysis. It combines several mathematical concepts to produce a system of linear and nonlinear equations. In the finite element formulation we assumed that the nature of the boundary conditions remains unchanged during the application of the load on the finite element assemblage. With these assumptions, the finite element equilibrium equations derived were for static analysis.

$$\mathbf{KU = R} \qquad (1)$$

These equations correspond to a linear analysis of a structure problem because the displacement response U is a linear function of the applied load vector R, if the

loads are αR instead of R, where α is a constant, the corresponding displacement are αU. When this is not case, we perform a nonlinear analysis.

A general nonlinear analysis is to find the state of equilibrium of a body corresponding to the applied loads. Assuming that the externally applied loads are described as a function of time, the equilibrium conditions of a system of finite elements representing the body under consideration can be expressed as

$$^{t}R - ^{t}F = 0 \tag{2}$$

where the vector ^{t}R lists the externally applied nodal point forces in the configuration at time t and the vector ^{t}F lists the nodal point forces that correspond to the element stresses in this configuration.

Basic equations to be solve in nonlinear analysis are, at time

$$^{t+\Delta t}R - ^{t+\Delta t}F = 0 \tag{3}$$

where the vector $^{t+\Delta t}R$ stores the externally applied nodal loads and $^{t+\Delta t}F$ is the vector of nodal point forces that are equivalent to the element stresses. Both vector R and F is evaluated using the principle of virtual displacements. Since the nodal point forces $^{t+\Delta t}F$ depend nonlinearly on the nodal point displacements, it is necessary to iterate in the solution of nonlinear analysis equation.

9.1 Newton-Raphson shemes

The most frequently used iteration schemes for the solution of nonlinear finite element equations are the Newton-Raphson iteration.

$$\Delta R^{(i-1)} = ^{t+\Delta t}R - ^{t+\Delta t}F^{(i-1)} \tag{4}$$

for i = 1, 2, 3,…

$$ {}^{t+\Delta t}K^{(i-1)}\Delta U^{(i)} = \Delta R^{(i-1)} \tag{5} $$

$$ {}^{t+\Delta t}U^{(i)} = {}^{t+\Delta t}U^{(i-1)} + U^{(i)} \tag{6} $$

With

$$ {}^{t+\Delta t}U^{(0)} = {}^{t}U\ ; \qquad {}^{t+\Delta t}F^{(0)} = {}^{t}F \tag{7} $$

These equations were obtained by linearizing the response of the finite element system about the conditions at time $t + \Delta t$, iteration $(i-1)$.

The finite element equilibrium requirements amount to finding the solution of the equations.

$$ f(U^*) = 0 \tag{8} $$

where

$$ f(U^*) = {}^{t+\Delta t}R(U^*) - {}^{t+\Delta t}F(U^*) \tag{9} $$

We denote here and in the following the complete array of the solution as U^* but realize that this vector may also contain variables other than displacements. Assume that in the iterative solution we have evaluated ${}^{t+\Delta t}U^{(i-1)}$; then a Taylor series expansion gives.

$$ f(U^*) = f({}^{t+\Delta t}U^{(i-1)}) + \left[\frac{\partial f}{\partial U}\right]_{{}^{t+\Delta t}U^{(i-1)}} (U^* - {}^{t+\Delta t}U^{(i-1)}) + \text{higher-order terms} \tag{10} $$

Substituting the equation, we obtain

$$\left[\frac{\partial F}{\partial U}\right]\Big|_{{}^{t+\Delta t}U^{(i-1)}} ({U}^{*}-{}^{t+\Delta t}U^{(i-1)}) + \text{higher-order terms} = {}^{t+\Delta t}R-{}^{t+\Delta t}F^{(i-1)} \qquad (11)$$

where we assumed that the externally applied loads are deformation-independent. Neglecting the higher-order terms, we can calculate an increment in the displacements,

$${}^{t+\Delta t}K^{(i-1)}\Delta U^{(i)} = {}^{t+\Delta t}R-{}^{t+\Delta t}F^{(i-1)} \qquad (12)$$

where ${}^{t+\Delta t}K^{(i-1)}$ is the current tangent stiffness matrix

$${}^{t+\Delta t}K^{(i-1)} = \left[\frac{\partial F}{\partial U}\right]\Big|_{{}^{t+\Delta t}U^{(i-1)}} \qquad (13)$$

and the improved displacement solution is

$${}^{t+\Delta t}U^{(i)} = {}^{t+\Delta t}U^{(i-1)} + \Delta U^{(i)} \qquad (14)$$

The relation of ${}^{t+\Delta t}K^{(i-1)}\Delta U^{(i)}$ and ${}^{t+\Delta t}U^{(i)}$ constitute the Newton-Raphson solution of ${}^{t+\Delta t}R-{}^{t+\Delta t}F = 0$. Since an incremental analysis is performed with time (or load) step of size Δt, the initial conditions in this iteration are ${}^{t+\Delta t}K^{(0)} = {}^{t}K$, ${}^{t+\Delta t}F^{(0)} = {}^{t}F$ and ${}^{t+\Delta t}U^{(0)} = {}^{t}U$. The iteration is continued until appropriate convergence criteria are satisfied. A characteristic of this iteration is that a new tangent stiffness matrix is calculated in each iteration, which is why this method is also referred to as the full Newton-Raphson method. We shall mention below methods in which a current tangent stiffness matrix is not used, and these techniques are therefore not full Newton-Raphson methods.

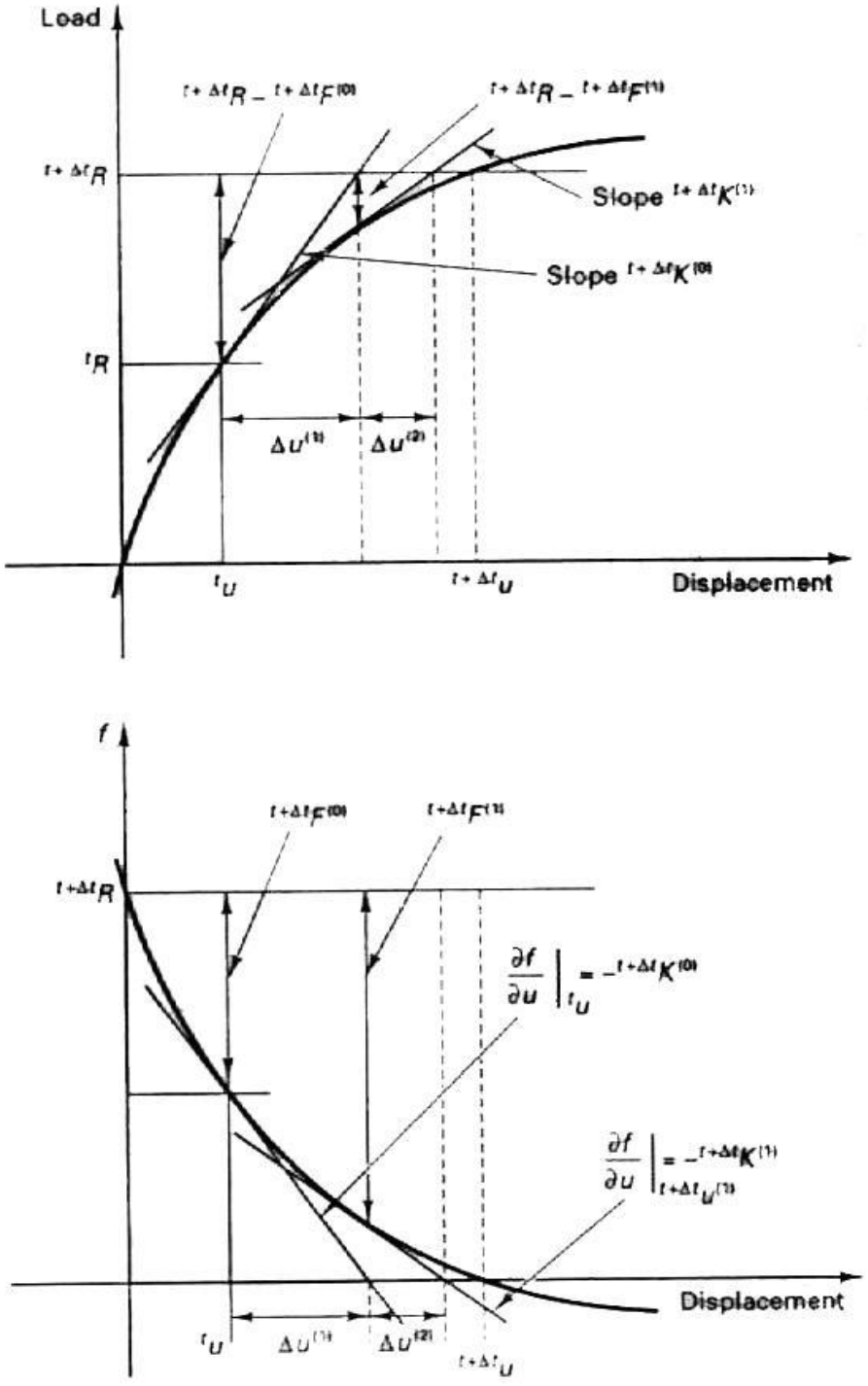

Figure 16 Illustration of Newton-Raphson iteration in solution of a single degree of freedom system. (Top) Shows load-displacement relation. (Bottom) Shows iteration for zero of function f used.

Source: Bath (1996).

Figure 16 illustrates the process of solution when used for a single degree of freedom system. The nonlinear response characteristics are such that convergence is rapidly obtained. However, we can imagine a more complex response characteristic with a starting point of iteration for which the procedure does not converge. Hence, the representation in Figure 16 is rather simplistic because a very special case is considered that of a well-behaved single degree of freedom system. In the solution of systems with many degree of freedom, the response curves will in general be rather non-smooth and complicated.

9.2 Element types used in the FEA simulation (Moaveni, 1999)

9.2.1 The Four-node tetrahedral element is the simplest three-dimensional element used in the analysis of solid mechanic problems. This element has four nodes, with each node having three translational degrees of freedom in the nodal x, y, and z-directions. A typical four-node tetrahedral element is shown in Figure 17.

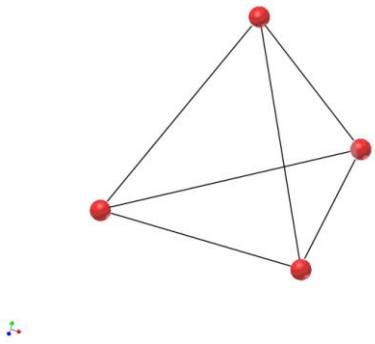

Figure 17 Four-node tetrahedral element.
Source: http://fea-cae-engineering.com (2009).

9.2.2 Ten-node tetrahedral is a higher order version of the three-dimensional linear tetrahedral element. It modified four nodes tetrahedral element by inserting mid-side nodes on each element edge. Consequently, the obtained result is more accurate than the four-node type due to the approximation method is second-order interpolation. A typical ten-node tetrahedral element is shown in Figure 18.

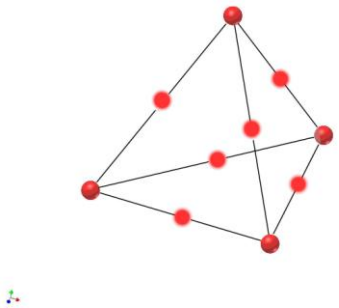

Figure 18 Ten-node tetrahedral element.
Source: http://fea-cae-engineering.com (2009).

9.2.3 Eight-node hexahedral is the next simple three-dimensional element used in the analysis of solid mechanics problem. Each of the eight nodes of this element has three translational degrees of freedom in the nodal x, y, and z-directions. A typical eight-node hexahedral element is shown in Figure 19.

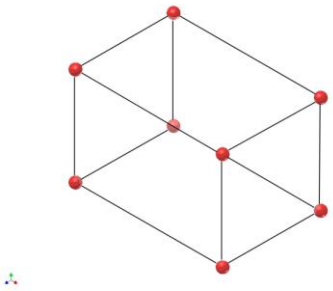

Figure 19 Eight-node hexahedral element.
Source: http://fea-cae-engineering.com (2009).

9.2.4 Twenty-node hexahedral is a higher order version of the three-dimensional eight-node brick element. This element is more capable and more accurate for modeling problem with curved boundaries than the eight-node brick element. A typical twenty-node hexahedral element is shown in Figure 20.

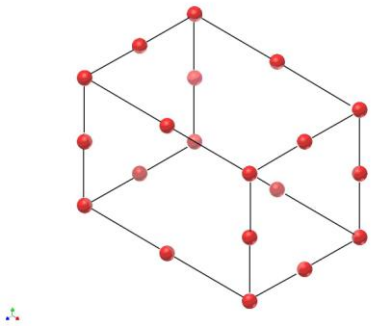

Figure 20 Twenty-node hexahedral element.
Source: http://fea-cae-engineering.com (2009).

9.3 Analysis of three-dimensional solid problem using four-node tetrahedral elements

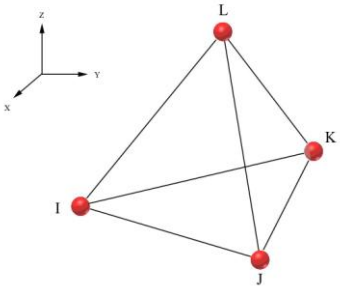

Figure 21 A four-node tetrahedral element.
Source: http://fea-cae-engineering.com (2009).

The shape functions for two-dimensional problems. The displacement field was represented by following equations:

$$u = C_{11} + C_{12}X + C_{13}Y + C_{14}Z \tag{15}$$

$$v = C_{21} + C_{22}X + C_{23}Y + C_{24}Z \tag{16}$$

$$w = C_{31} + C_{32}X + C_{33}Y + C_{34}Z \tag{17}$$

Considering the nodal displacements, we must satisfy the following conditions:

$$\begin{array}{llllllll}
u = u_I & \text{at} & X = X_I & Y = Y_I & \text{and} & Z = Z_I \\
u = u_J & \text{at} & X = X_J & Y = Y_J & \text{and} & Z = Z_J \\
u = u_K & \text{at} & X = X_K & Y = Y_K & \text{and} & Z = Z_K \\
u = u_L & \text{at} & X = X_L & Y = Y_L & \text{and} & Z = Z_L
\end{array}$$

Similarly, we must satisfy the following requirements:

$$\begin{array}{llllllll}
v = v_I & \text{at} & X = X_I & Y = Y_I & \text{and} & Z = Z_I \\
\vdots & \vdots & \vdots & \vdots & \vdots & \vdots \\
w = w_L & \text{at} & X = X_I & Y = Y_I & \text{and} & Z = Z_I
\end{array}$$

Substitution of respective nodal values into equations u, v, and w result in 12 equations and 12 unknowns:

$$\begin{array}{c}
u_I = C_{11} + C_{12}X_I + C_{13}Y_I + C_{14}Z_I \\
u_J = C_{11} + C_{12}X_J + C_{13}Y_J + C_{14}Z_J \\
\vdots \\
w_L = C_{31} + C_{32}X_L + C_{33}Y_L + C_{34}Z_L
\end{array} \tag{18}$$

Solving for the unknown C-coefficients, substituting the result back into equations u, v, and w and regrouping the parameters, we obtain:

$$u = S_1 u_I + S_2 u_J + S_3 u_K + S_4 u_L \tag{19}$$

$$v = S_1 v_I + S_2 v_J + S_3 v_K + S_4 v_L \tag{20}$$

$$w = S_1 w_I + S_2 w_J + S_3 w_K + S_4 w_L \tag{21}$$

The shape functions are

$$S_1 = \frac{1}{6V}\left(a_I + b_I X + c_I Y + d_I Z\right) \tag{22}$$

$$S_2 = \frac{1}{6V}\left(a_J + b_J X + c_J Y + d_J Z\right) \tag{23}$$

$$S_3 = \frac{1}{6V}\left(a_K + b_K X + c_K Y + d_K Z\right) \tag{24}$$

$$S_4 = \frac{1}{6V}\left(a_L + b_L X + c_L Y + d_L Z\right) \tag{25}$$

where V, the volume of the tetrahedral element, is computed from

$$6V = \det\begin{vmatrix} 1 & X_I & Y_I & Z_I \\ 1 & X_J & Y_J & Z_J \\ 1 & X_K & Y_K & Z_K \\ 1 & X_L & Y_L & Z_L \end{vmatrix} \tag{26}$$

the $a_I, b_I, c_I, d_I, \ldots,$ and d_L -terms are:

$$a_I = \det\begin{vmatrix} X_J & Y_J & Z_J \\ X_K & Y_K & Z_K \\ X_L & Y_L & Z_L \end{vmatrix} \tag{27}$$

$$b_I = -\det\begin{vmatrix} 1 & Y_J & Z_J \\ 1 & Y_K & Z_K \\ 1 & Y_L & Z_L \end{vmatrix} \tag{28}$$

$$c_I = \det\begin{vmatrix} X_J & 1 & Z_J \\ X_K & 1 & Z_K \\ X_L & 1 & Z_L \end{vmatrix} \tag{29}$$

$$d_I = -\det\begin{vmatrix} X_J & Y_J & 1 \\ X_K & Y_K & 1 \\ X_L & Y_L & 1 \end{vmatrix} \tag{30}$$

We can present the $a_J, b_J, c_J, d_J, \ldots,$ and d_L-terms using similar determinants by rotating through the I, J, K, and L subscripts using the right-hand rule.

$$a_J = \det\begin{vmatrix} X_K & Y_K & Z_K \\ X_L & Y_L & Z_L \\ X_I & Y_I & Z_I \end{vmatrix} \tag{31}$$

The six independent stress components are needed to characterize the general state of stress at a point. These components are

$$[\sigma]^T = \begin{bmatrix} \sigma_{xx} & \sigma_{yy} & \sigma_{zz} & \tau_{xy} & \tau_{yz} & \tau_{xz} \end{bmatrix} \tag{32}$$

The displacement vector measured the change occurring in the position of a point within a body when the body is subjected to a load. The displacement vector, $\vec{\delta}$ can be written in terms of its Cartesian components as

$$\vec{\delta} = u(x,y,z)\vec{i} + v(x,y,z)\vec{j} + w(x,y,z)\vec{k} \tag{33}$$

The general state of strain is characterized by six independent components as given by

$$[\varepsilon]^T = \begin{bmatrix} \varepsilon_{xx} & \varepsilon_{yy} & \varepsilon_{zz} & \gamma_{xy} & \gamma_{yz} & \gamma_{xz} \end{bmatrix} \tag{34}$$

The relationship between the strain and the displacement is presented by

$$\varepsilon_{xx} = \frac{\partial u}{\partial x} \qquad \varepsilon_{yy} = \frac{\partial v}{\partial y} \qquad \varepsilon_{zz} = \frac{\partial w}{\partial z} \tag{35}$$

$$\gamma_{xy} = \frac{\partial u}{\partial y} + \frac{\partial v}{\partial x} \qquad \gamma_{yz} = \frac{\partial v}{\partial z} + \frac{\partial w}{\partial y} \qquad \gamma_{xz} = \frac{\partial u}{\partial z} + \frac{\partial w}{\partial x} \tag{36}$$

It can be represented in matrix form as

$$\{\varepsilon\} = LU \tag{37}$$

where

$$\{\varepsilon\} = \begin{Bmatrix} \varepsilon_{xx} \\ \varepsilon_{yy} \\ \varepsilon_{zz} \\ \gamma_{xy} \\ \gamma_{yz} \\ \gamma_{xz} \end{Bmatrix} \tag{38}$$

and

$$LU = \begin{Bmatrix} \dfrac{\partial u}{\partial x} \\ \dfrac{\partial v}{\partial y} \\ \dfrac{\partial w}{\partial z} \\ \dfrac{\partial u}{\partial y} + \dfrac{\partial v}{\partial x} \\ \dfrac{\partial v}{\partial z} + \dfrac{\partial w}{\partial y} \\ \dfrac{\partial w}{\partial x} + \dfrac{\partial u}{\partial z} \end{Bmatrix} \tag{39}$$

L is commonly referred to as the linear differential operator.

Over the elastic region of a material, there also exists a relationship between the state of stresses and strains, according to the generalized Hooke's Law. This relationship is given by the following equations:

$$\varepsilon_{xx} = \frac{1}{E}\left[\sigma_{xx} - \nu\left(\sigma_{yy} + \sigma_{zz}\right)\right] \tag{40}$$

$$\varepsilon_{yy} = \frac{1}{E}\left[\sigma_{yy} - \nu\left(\sigma_{xx} + \sigma_{zz}\right)\right] \tag{41}$$

$$\varepsilon_{zz} = \frac{1}{E}\left[\sigma_{zz} - \nu\left(\sigma_{xx} + \sigma_{yy}\right)\right] \tag{42}$$

$$\gamma_{xy} = \frac{1}{G}\tau_{xy} \qquad \gamma_{yz} = \frac{1}{G}\tau_{yz} \qquad \gamma_{zx} = \frac{1}{G}\tau_{zx} \tag{43}$$

The relationship between the stress and strain can be expressed in a compact-matrix form as:

$$\{\sigma\} = [\nu]\{\varepsilon\} \tag{44}$$

where

$$\{\sigma\} = \begin{Bmatrix} \sigma_{xx} \\ \sigma_{yy} \\ \sigma_{zz} \\ \tau_{xy} \\ \tau_{yz} \\ \tau_{xz} \end{Bmatrix} \tag{45}$$

$$[v]=\frac{E}{1+v}\begin{bmatrix} \frac{1-v}{1-2v} & \frac{v}{1-2v} & \frac{v}{1-2v} & 0 & 0 & 0 \\ \frac{v}{1-2v} & \frac{1-v}{1-2v} & \frac{v}{1-2v} & 0 & 0 & 0 \\ \frac{v}{1-2v} & \frac{v}{1-2v} & \frac{1-v}{1-2v} & 0 & 0 & 0 \\ 0 & 0 & 0 & \frac{1}{2} & 0 & 0 \\ 0 & 0 & 0 & 0 & \frac{1}{2} & 0 \\ 0 & 0 & 0 & 0 & 0 & \frac{1}{2} \end{bmatrix} \tag{46}$$

$$\{\varepsilon\}=\begin{Bmatrix} \varepsilon_{xx} \\ \varepsilon_{yy} \\ \varepsilon_{zz} \\ \gamma_{xy} \\ \gamma_{yz} \\ \gamma_{xz} \end{Bmatrix}$$

For a solid material under tri-axial loading, the strain energy Λ is

$$\Lambda^{(e)}=\frac{1}{2}\int_V\left(\sigma_{xx}\varepsilon_{xx}+\sigma_{yy}\varepsilon_{yy}+\sigma_{zz}\varepsilon_{zz}+\tau_{xy}\gamma_{xy}+\tau_{xz}\gamma_{xz}+\tau_{yz}\gamma_{yz}\right)dV \tag{47}$$

Or, in a compact-matrix form,

$$\Lambda^{(e)}=\frac{1}{2}\int_V\{\varepsilon\}^T[v]\{\varepsilon\}dV \tag{48}$$

We will now use the four-node tetrahedral element to formulate the stiffness matrix. Recall that this element has four nodes, with each node having three

translational degrees of freedom in the nodal x, y, and z-direction. The displacements u, v, and w in terms of the nodal values and the shapes functions are represented by

$$\{\mathrm{u}\} = [S]\{U\} \tag{49}$$

where

$$\{\mathrm{u}\} = \begin{Bmatrix} u \\ v \\ w \end{Bmatrix} \tag{50}$$

$$[S] = \begin{bmatrix} S_1 & 0 & 0 & S_2 & 0 & 0 & S_3 & 0 & 0 & S_4 & 0 & 0 \\ 0 & S_1 & 0 & 0 & S_2 & 0 & 0 & S_3 & 0 & 0 & S_4 & 0 \\ 0 & 0 & S_1 & 0 & 0 & S_2 & 0 & 0 & S_3 & 0 & 0 & S_4 \end{bmatrix} \tag{51}$$

$$\{U\} = \begin{Bmatrix} u_I \\ v_I \\ w_I \\ u_J \\ v_J \\ w_J \\ u_K \\ v_K \\ w_K \\ u_L \\ v_L \\ w_L \end{Bmatrix} \tag{52}$$

The next steps, we begin by relating the strains to the displacement field and, in turn, to the nodal displacements through the shape functions. We need to take the

derivatives of the components of the displacement field with respect to x, y, and z-coordinates according to the strain-displacement relation. The operation result in:

$$\begin{Bmatrix} \varepsilon_{xx} \\ \varepsilon_{yy} \\ \varepsilon_{zz} \\ \gamma_{xy} \\ \gamma_{yz} \\ \gamma_{xz} \end{Bmatrix} = \begin{bmatrix} \frac{\partial S_1}{\partial x} & 0 & 0 & \frac{\partial S_2}{\partial x} & 0 & 0 & \frac{\partial S_3}{\partial x} & 0 & 0 & \frac{\partial S_4}{\partial x} & 0 & 0 \\ 0 & \frac{\partial S_1}{\partial y} & 0 & 0 & \frac{\partial S_2}{\partial y} & 0 & 0 & \frac{\partial S_3}{\partial y} & 0 & 0 & \frac{\partial S_4}{\partial y} & 0 \\ 0 & 0 & \frac{\partial S_1}{\partial z} & 0 & 0 & \frac{\partial S_2}{\partial z} & 0 & 0 & \frac{\partial S_3}{\partial z} & 0 & 0 & \frac{\partial S_4}{\partial z} \\ \frac{\partial S_1}{\partial y} & \frac{\partial S_1}{\partial x} & 0 & \frac{\partial S_2}{\partial y} & \frac{\partial S_2}{\partial x} & 0 & \frac{\partial S_3}{\partial y} & \frac{\partial S_3}{\partial x} & 0 & \frac{\partial S_4}{\partial y} & \frac{\partial S_4}{\partial x} & 0 \\ 0 & \frac{\partial S_1}{\partial z} & \frac{\partial S_1}{\partial y} & 0 & \frac{\partial S_2}{\partial z} & \frac{\partial S_2}{\partial y} & 0 & \frac{\partial S_3}{\partial z} & \frac{\partial S_3}{\partial y} & 0 & \frac{\partial S_4}{\partial z} & \frac{\partial S_4}{\partial y} \\ \frac{\partial S_1}{\partial z} & 0 & \frac{\partial S_1}{\partial x} & \frac{\partial S_2}{\partial Z} & 0 & \frac{\partial S_2}{\partial x} & \frac{\partial S_3}{\partial z} & 0 & \frac{\partial S_3}{\partial x} & \frac{\partial S_4}{\partial z} & 0 & \frac{\partial S_4}{\partial x} \end{bmatrix} \tag{53}$$

substituting for the shape functions and differentiating, we have

$$\{\varepsilon\} = [B]\{U\} \tag{54}$$

where

$$[B] = \frac{1}{6V} \begin{bmatrix} b_I & 0 & 0 & b_J & 0 & 0 & b_K & 0 & 0 & b_L & 0 & 0 \\ 0 & c_I & 0 & 0 & c_J & 0 & 0 & c_K & 0 & 0 & c_L & 0 \\ 0 & 0 & d_I & 0 & 0 & d_J & 0 & 0 & d_K & 0 & 0 & d_L \\ c_I & b_I & 0 & c_J & b_J & 0 & c_K & b_K & 0 & c_L & b_L & 0 \\ 0 & d_I & c_I & 0 & d_J & c_J & 0 & d_K & c_K & 0 & d_L & c_L \\ d_I & 0 & b_I & d_J & 0 & b_J & d_K & 0 & b_K & d_L & 0 & b_L \end{bmatrix} \tag{55}$$

and the volume V and the b, c, and d-terms are given. Substituting into the strain energy equation for the strain components in terms of the displacements, we obtain

$$\Lambda^{(e)} = \frac{1}{2}\int_V \{\varepsilon\}^T [v]\{\varepsilon\} dV = \frac{1}{2}\int_V [U]^T [B]^T [v][B][U] dV \qquad (56)$$

Differentiating with respect to the nodal displacements yields

$$\frac{\partial \Lambda^{(e)}}{\partial U_k} = \frac{\partial}{\partial U_k}\left(\frac{1}{2}\int_V [U]^T [B]^T [v][B][U] dV\right) \qquad \text{for k = 1, 2, …, 12} \qquad (57)$$

Evaluation of the equation $\frac{\partial \Lambda^{(e)}}{\partial U_k}$ results in the expression $[K]^{(e)}\{U\}$ and, subsequently, the expression for the stiffness matrix, which is

$$[K]^{(e)} = \int_V [B]^T [v][B] dV = V[B]^T [v][B] \qquad (58)$$

where V is the volume of the element. The resulting stiffness matrix will have the dimension of 12x12.

9.4 Load matrix

The load matrix for a tetrahedral element is a 12x1 matrix. For a concentrated-loading situation, the load matrix is formed by placing the components of the load at appropriate nodes in appropriate directions. For a distributed load, the load matrix is computed from the equation

$$\{F\}^{(e)} = \int_A [S]^T \{p\} dA \qquad (59)$$

where

$$\{p\} = \begin{Bmatrix} p_x \\ p_y \\ p_z \end{Bmatrix} \tag{60}$$

and A represents the surface over which the distributed-load components are acting. The surfaces of the tetrahedral element are triangular in shape. Assuming that the distributed load acts on the I-J-K surfaces, the load matrix becomes:

$$\{F\}^{(e)} = \frac{A_{I-J-K}}{3} \begin{Bmatrix} p_x \\ p_y \\ p_z \\ p_x \\ p_y \\ p_z \\ p_x \\ p_y \\ p_z \\ 0 \\ 0 \\ 0 \end{Bmatrix} \tag{61}$$

The load matrix for distributed load acting on the other surfaces of the tetrahedral element is obtained in a similar fashion.

10. Related research

Boileau and Walch (1997) studied the three-dimensional geometry of the proximal humerus on human cadaver specimens using a digitized measuring device linked to a computer. Our findings demonstrated the variable shape of the proximal humerus as well as its variable dimensions. The articular surface, which is part of a sphere, varies individually in its orientation as regards inclination and retroversion, and it has variable medial and posterior offsets. These variations cannot be accommodated by the designs of most contemporary humeral components. Although good clinical results can be achieved with current modular and non-modular components their relatively.

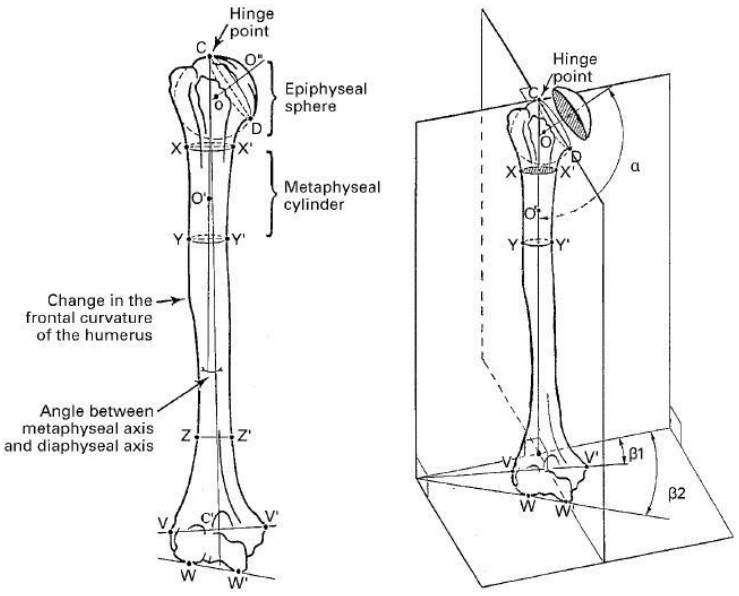

(A) (B)

Figure 22 (A) Axes used to characterise the morphological factors: (1) humeral head axis; (2) diaphyseal axis; (3) metaphyseal axis; (4) transepicondylar axis; (5) tangent elbow axis. (B) Three-dimensional co-ordinate system.

Source: Boileau and Walch (1997).

Fixed geometry prevents truly anatomical restoration in many cases. To try to restore the original three-dimensional geometry of the proximal humerus, we have developed a new type of humeral component which is modular and adaptable to the individual anatomy. Such adaptability allows correct positioning of the prosthetic head in relation to an individual anatomical neck, after removal of the marginal osteophytes. The design of this third generation prosthesis respects the four geometrical variations which have been demonstrated in the present study. These are inclination, retroversion, medial offset and posterior offset.

Akpinar *et al*. (2003) reported that there are many problems in intramedullary humeral stabilization because of the anatomic structure of the bone. They performed various methods and measurements to determine shape, length and diameter and curvature of the medullary canal of the humerus in 57 human dry cadaver bones.

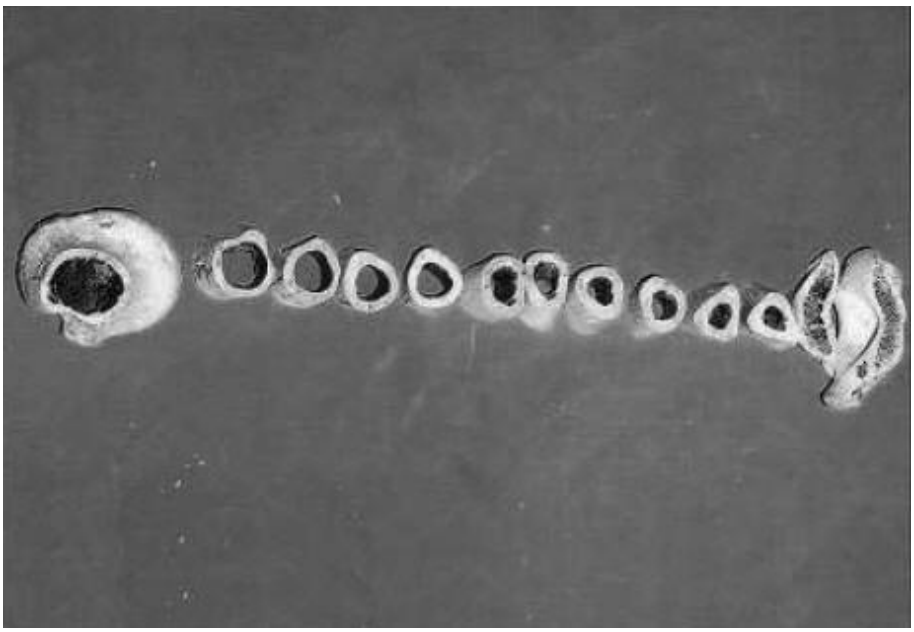

Figure 23 Photograph showing increasing diameter of medullary canal from distal to proximal.

Source: Akpinar *et al*. (2003).

Anterior angulation with an average of 21 cm apart from greater tubercle was found at 1/3 distal part. Mean degree of angulation was 9° (max: 15, minutes: 5, S.D.: 2.84). Humerus bones with septal aperture (supratrochlear foramen) at the fossa coronoidea were observed to have very narrow medullary canal.

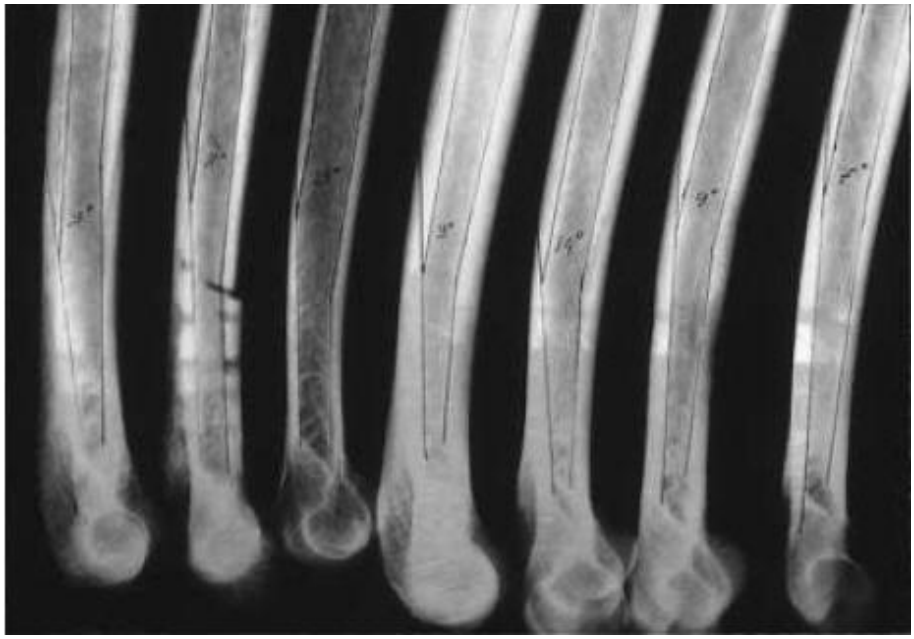

Figure 24 Lateral radiological view showing anterior angulations.
Source: Akpinar *et al*. (2003).

The best point for nail insertion was found to be an area on the line from greater tubercle anteromedially to caput humeri. This study revealed that carefully evaluated structure of humeral medullary canal and various congenital constructions such as septal aperture, and correct selection of a nail with proper length and diameter are essential for successful nailing.

Maldonado *et al*. (2003) hypothesized that the bone quality has a high influence on the bone straining, independent of the arm position. The goal of this study was to determine the straining of the intact and fractured proximal humerus under physiological-like loading conditions. Furthermore, the impact of augmentation on tissue straining was evaluated. Two representative humeri were selected for this

study, one osteoporotic and one reference quality, and scanned using both QCT and DEXA (average DEXA value=0.26 and 0.49 g/cm2 respectively). Subcaptial defects were generated, then stabilized with a plate prior to mechanical stiffness testing. From the QCT data, finite element models were generated and the in vitro stiffness tests analytically simulated. Under physiological-like loading conditions, the straining of the bone and implant were analyzed for 0°, 90° forward flexion, and 90° abduction.

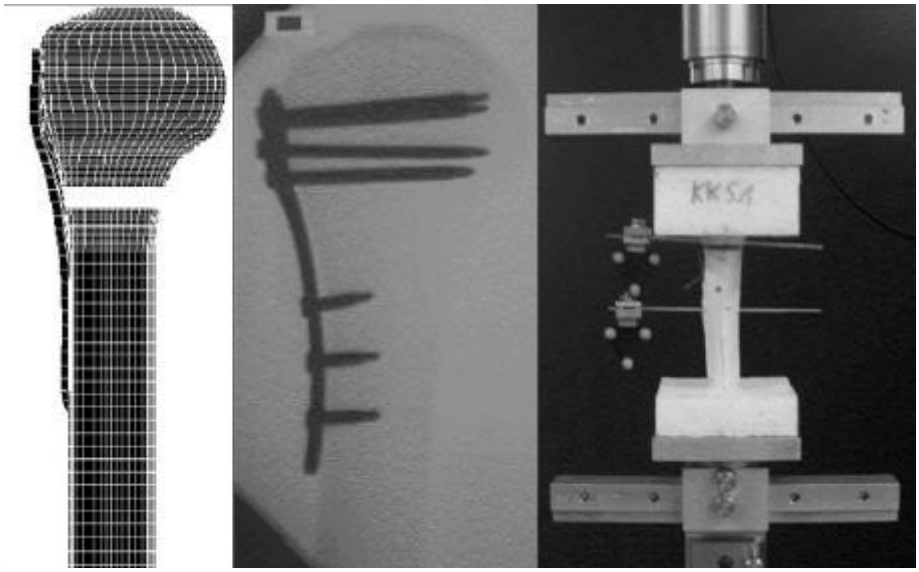

Figure 25 Proximal humerus with defect localization and a LCP-PH implant under compressive loads. Left: Finite element model of the proximal humerus with implant. Middle: X-ray of a specimen with implant but prior to the osteotomy. Right: Specimen in material testing machine under pure compression. Reflective markers (distance between marker trees=60mm) are attached to each segment to allow determination of the interfragmentary movements. From these movements and loads, the stiffness of the bone implant construct was computed.

Source: Maldonado *et al*. (2003).

Maximal strain values were found for the intact and fractured bone at 90 degree abduction. This study demonstrates that the straining in a fractured bone of poor quality leads to considerably higher bone strains (up to +30%) than in a more

healthy bone. Augmentation of a central void under physiological-like loading with commercial cement led to mechanical failure at the bone–cement interface.

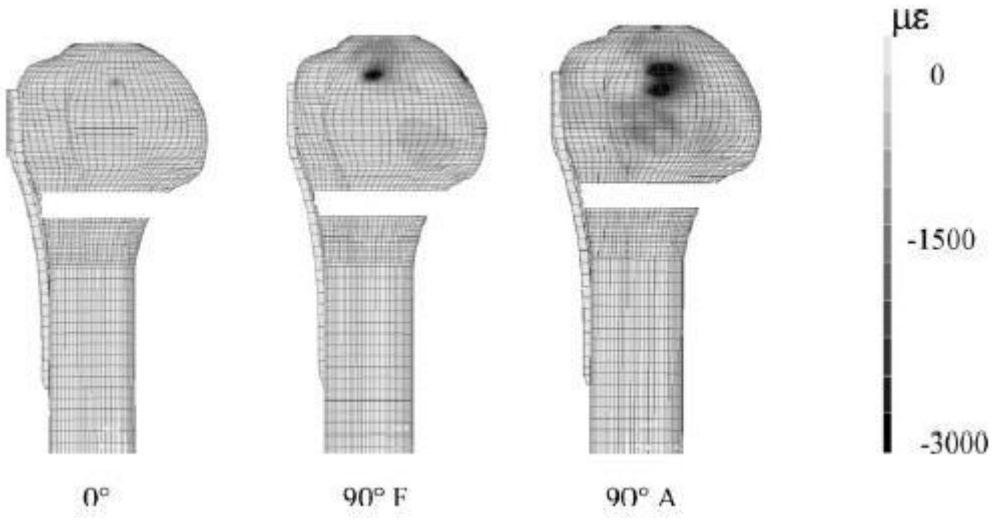

Figure 26 Minimum principle strains at the anterior bone surface. Osteoporotic, poor quality bone with a bone defect stabilized by an angle stable osteosynthetic device is shown for three different arm positions: 0°, 90° forward flexion(F) and 90° abduction(A).

Source: Maldonado *et al*. (2003).

New concepts for the surgical treatment of complex fractures of the proximal humerus should take bone distribution into account and thereby allow effective treatment of fractures in osteoporotic patients. The ultimate salvage procedure of augmentation has mechanical limitations as long as current cement materials are used in osteoporotic patients.

Mahaisavariya *et al.* (2004) studied a three-dimensional virtual simulation method to evaluate the fit-and-fill effect of the insertion of a trochanteric gamma nail (TGN) in 98 Thai dadaveric proximal femora.

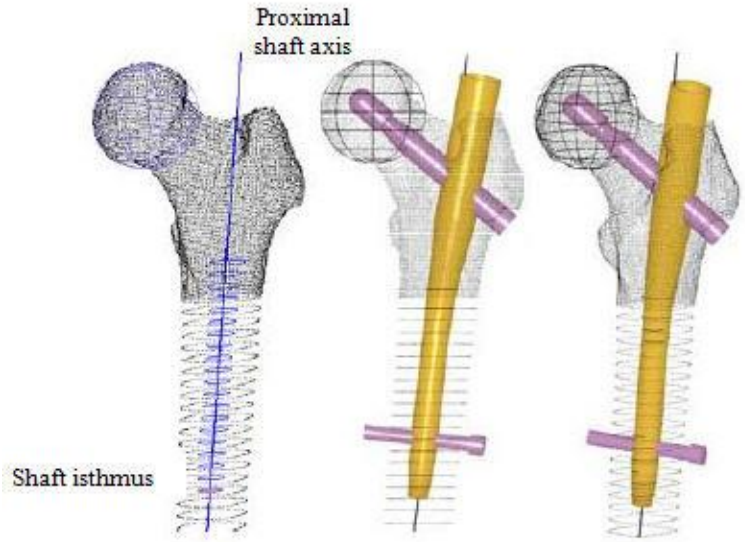

Figure 27 The insertion of a TGN into the 3D proximal femur derived from CT images.

Source: Mahaisavariya *et al.* (2004).

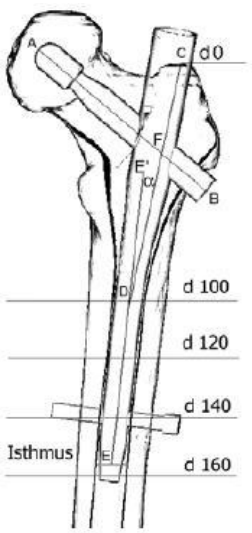

Figure 28 The diagram of fit and fill study of the TGN in the proximal femur.

Source: Mahaisavariya *et al.* (2004).

The circular best fit of the 2-dimensional cross-section of the femoral canal and the nail at 4 levels [d100, d120, d140 and d160] which were located at 100, 120, 140 and 160 mm distal to the tip of the greater trochanter were calculated (Figure 22 and 23). The evaluation of each level included; 1) the diameters of the medullary canal, 2) the percentage of area filled by the nail in the unreamed medullary canal, 3) the minimal reamer diameter that required enlargement of the canal to accommodate TGN insertion, 4) the minimal inner cortical reaming thickness that needed to be removed, 5) the percentage of cortical bone area that needed to be removed prior to nail insertion and 6) the deviation of the nail center from the center of the medullary canal were presented as shown in Figure 29.

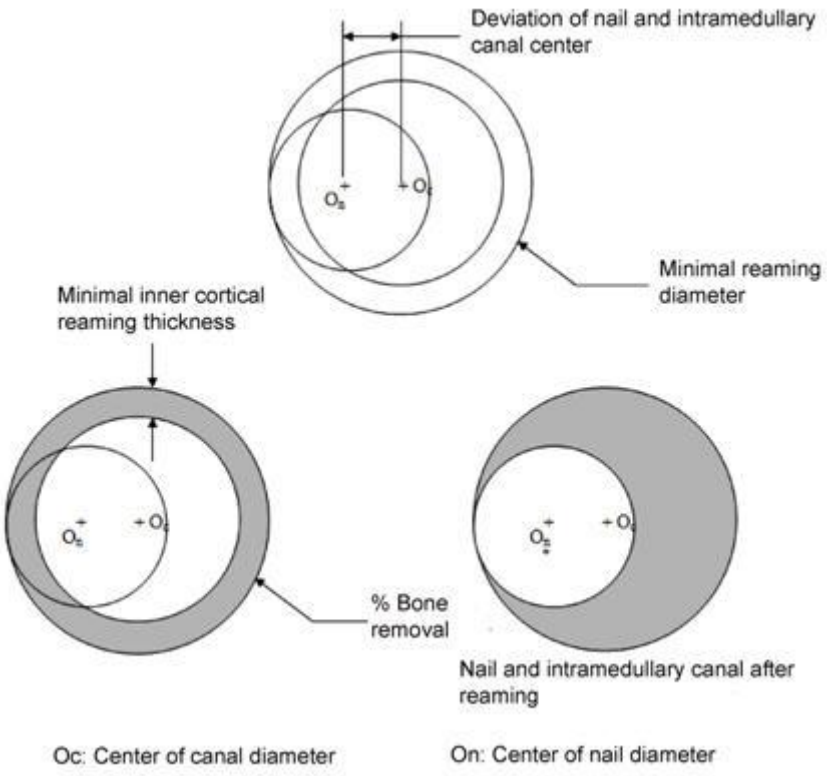

Figure 29 The calculated parameters for the evaluation of the fit and fill analysis.

The results showed that at 4 studied locations the diameter of unreamed medullary canal averaged 10.3 to 11.8 mm. The nail cross-section that could fill the medullary canal averaged 86.9-95.1%. The minimal reaming diameter for the medullary canal to accommodate the TGN insertion averaged 11.3 to 12.3 mm. The inner cortical thickness that should be removed averaged 0.6 to 0.8 mm. The cortical bone that needed to be removed averaged 13.6 to 19.3% of the total cortical area. The deviation of the nail center from the canal center averaged 0.3 to 0.8 mm. The present study showed some mismatching of the TGN to that of the Thai proximal femur. Appropriate reaming to prepare the medullary canal should be considered prior to TGN insertion to prevent technical problem. Future re-design of the implant may be considered for Thai patients.

MATERIALS AND METHOD

1. Geometric Mismatch of Humeral Nail with Antegrade versus Retrograde Insertion in Asian Humerus: A Virtual Simulation Study

1.1 Three-dimensional modeling

76 Asian humeri (38 rights and 38 lefts) from the previous study of cadaveric humeral database (Aroonjarutthum *et al.*, 2006) were used to investigate the virtual simulation of humeral nail insertion. The donor ages ranged from 22 to 79 years (average, 47.71) at the time of death. CT sections were available for the humeral bone with a spacing of 0.625-mm slice thickness. These specimens had all soft tissues removed and without previous surgery, trauma or arthritis. The scanning data were exported in the DICOM format file.

The scanning data were imported into a medical image processing software (Mimic, Materialise N.V., Belgium), and contours were generated for outer and inner cortices by use of thresholding techniques to differentiate between bone and soft tissue based on tissue mineral density. The optimal contours (outer and inner cortices) were exported into a steriolithography (STL) format. The standard humeral nail was created by Kreon KZ50 3D Laser Scanner combined with articulated arm Cimcore 3000i to perform the cloud point collection and was exported into the STL format.

1.2 Anatomic measurement technique

The 3-D reverse engineering technique was applied for anatomic measurement of a three dimensional reconstructed humerus obtained from CT medical images and imported into a computer aided design (CAD) software for analysis. To determine the **M**edullary **C**anal **A**xis, 20 cross sections of the humeral shaft were analyzed. The cross sections started at 50-mm below the highest point in proximal to distal direction (Figure 30). Each cross section was fitted with circle using

a least squares circle-fitting routine, and a line passed through centers of each cross section was a so-called "**M**edullary **C**anal **A**xis (MCA)".

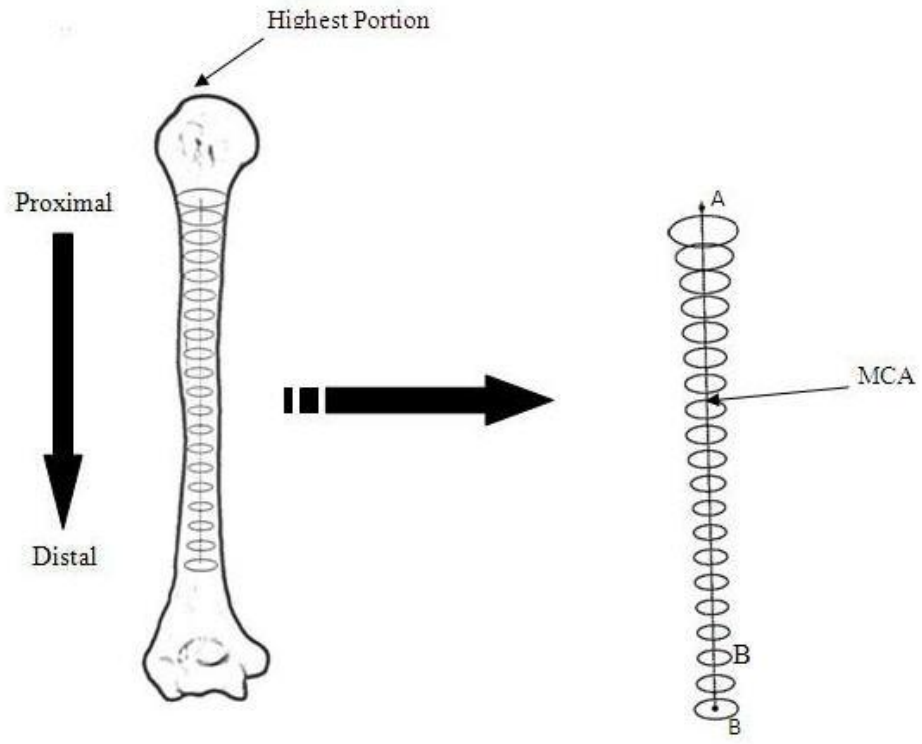

Figure 30 Cross sections of humeral medullary canal were used to create the medullary canal axis (MCA).

The Humeral Head Axis was derived from the geometric center of the humeral head and anatomical neck. The humeral head was evaluated as a sphere with a least-square sphere fit method, from this sphere the Humeral Head Center (HHC) was obtained. The anatomical neck was estimated as a circle by best fitting circle with minimum error at the narrowest portion, from this circle the Anatomical Neck Center (ANC) and entry point were obtained. Since the circle was located in three dimensional co-ordinate, the highest point of circle in proximal to distal direction was defined as "*Entry point*". The obtained centers of the humeral head and anatomical

neck were connected and the derivable line was defined as the "*Humeral Head Axis (HHA)*" (Figure 31).

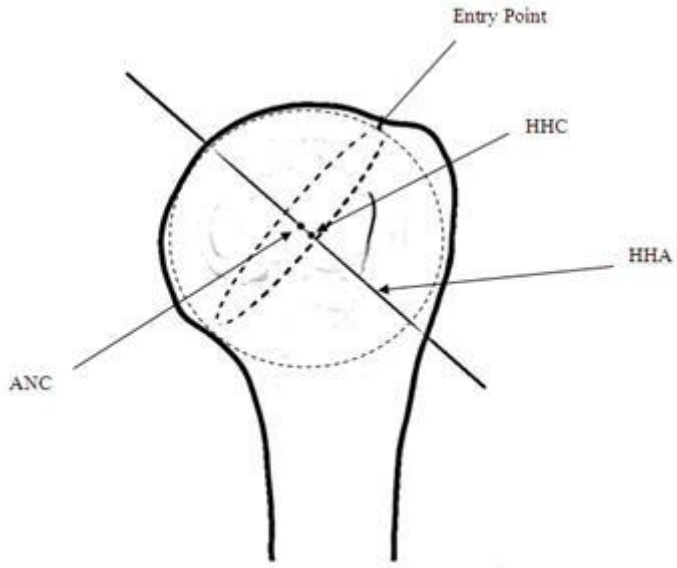

Figure 31 The proximal humerus with the parameters of humeral head.

In distal humerus portion, the olecranon fossa was evaluated as a sphere by selecting points from posterior side. The chosen points were located around fossa which was drawn as a closed loop. A least square fit method was used to determine the geometric center of the olecranon fossa which was defined as "*Fossa Center*" (Figure 32).

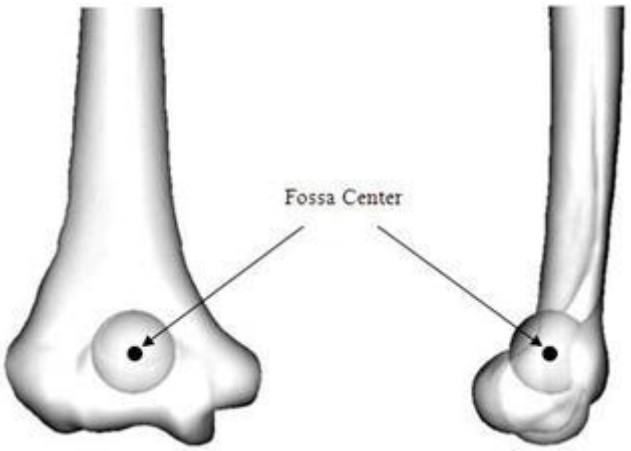

Figure 32 The best fit sphere of the olecranon fossa

1.3 Implant measurement technique

The reverse engineering method was applied for collecting parameters of a three dimensional reconstructed implant derived from laser scan images and imported into a CAD software for analysis. Twenty circular cross sections of the nail contour were analyzed to find out the **N**ail **S**haft **A**xis. The cross sections performed thoroughly the nail (Figure 33). Each cross section was fitted with circle using a least squares circle-fitting routine, and a line passed through centers of each circular cross section was "**N**ail **S**haft **A**xis (NSA)".

1.4 Significance plane

From anatomic measurement the significant three points were obtained: The end points of MCA (point A and B; Figure 30) and the entry point (Figure 31). These three points were used to generate the plane defined as "*Antegrade Plane*" (Figure 34). Both end points of MCA (Point A and B) and fossa center point were used to generate the plane defined as "*Retrograde Plane*". The NSA was analyzed by a least square fit geometry method to determine "*Nail Plane*" (Figure 34).

1.5 A virtual simulation

The 3-D reverse engineering technique was used to insert a humeral nail into the humerus model.

1.5.1 Antegrade insertion

(a) First step was to align the NSA of the humeral nail with the MCA by best fit function.

(b) Second step was to translate the NSA of the humeral nail along to MCA until the proximal end region of nail was passed through the humeral head.

(c) The final step was to rotate the nail plane and the antegrade plane until it was coincident.

1.5.2 Retrograde insertion

(a) First step was to align the NSA of the humeral nail with the MCA by best fit function. The humeral nail was in a reversed direction of antegrade insertion.

(b) Second step was to translate the NSA along to MCA until the proximal end of nail was located above the olecranon fossa 5-mm.

(c) The final step was to rotate the nail plane and retrograde plane until it was coincident.

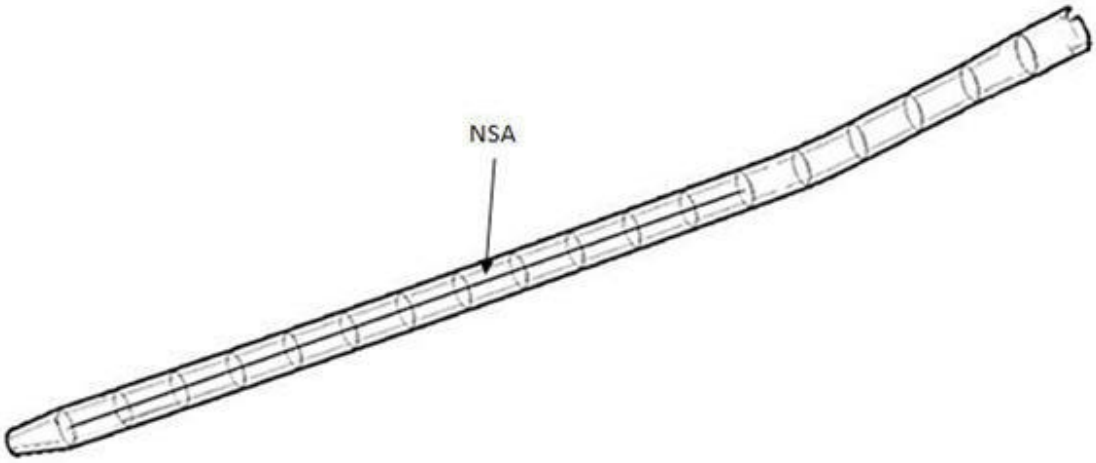

Figure 33 The circular cross section of the humeral nail with Nail Shaft Axis (NSA).

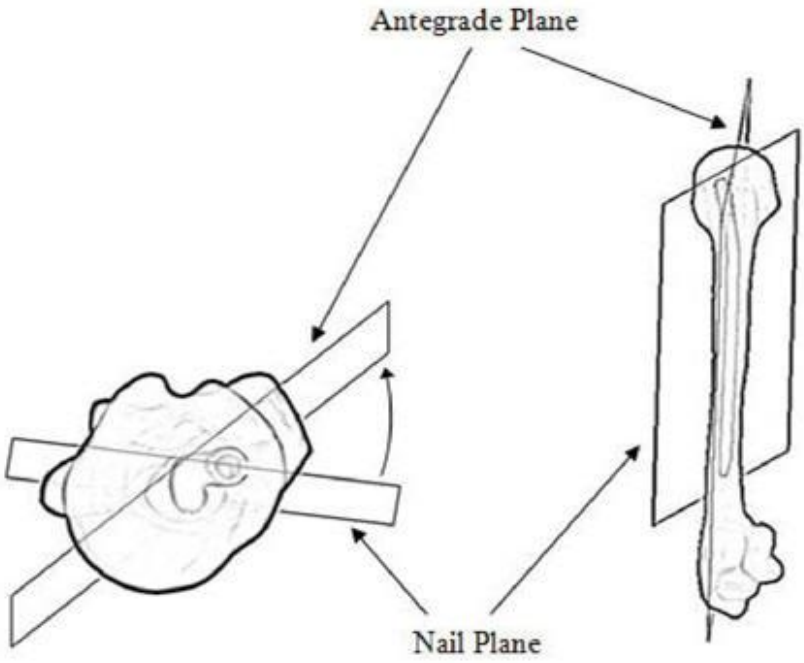

Figure 34 The antegrade insertion was shown as optimal position with two planes coincident.

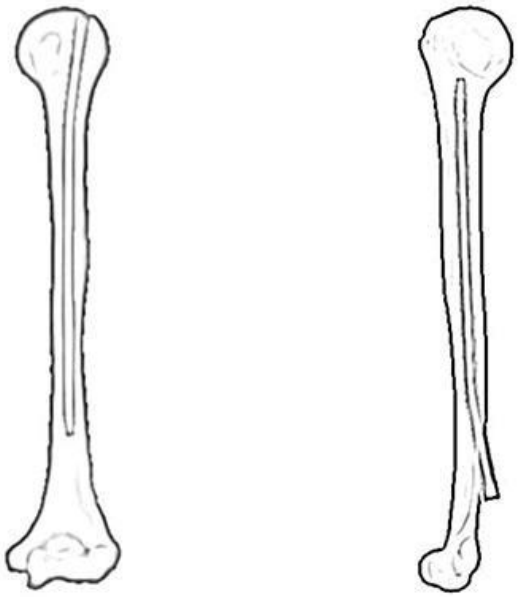

A) Antegrade insertion B) Retrograde insertion

Figure 35 The optimal position of antegrade and retrograde insertion with nail.

Considered intramedullary canal and humeral nail, cross-sectional of bone at 50 mm. (beginning of medullary canal) to 280 mm. (end of medullary canal) with 10-mm interval from proximal to distal part were created. Each section showed the circumference of nail and medullary canal (Figure 36).

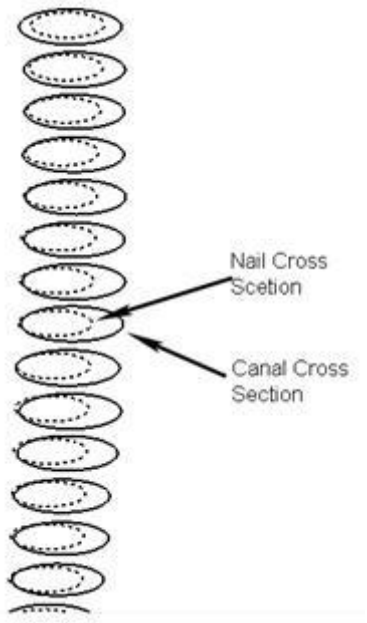

Figure 36 Circular cross-section of medullary canal and nail.

From the circular best fit of each section the data were collected as follows: 1) diameter of the medullary canal, 2) minimal reaming diameter to accommodate the nail insertion virtually, 3) minimal reaming thickness of the inner cortex, 4) percentage of cortical bone removal prior to nail insertion and 5) eccentric of the nail-medullary canal center. All parameters were calculated by using equation 62-65 and were shown in Figure 37 (Mahaisavariya *et al*., 2004).

Minimal reaming diameter

$$= 2 \times (\text{Radius}_{\text{canal}} + \text{Distance}_{\text{out of centricity}}) \quad (62)$$

Minimal inner cortical reaming thickness

$$= (\text{Minimal reaming dia.} - \text{Medullary canal dia.})/2 \quad (63)$$

% Bone removal

$$= \%[(\text{Area}_{\text{minimal reaming}} - \text{Area}_{\text{canal}})/\text{Area}_{\text{canal}} \quad (64)$$

The deviation of the nail center from the canal center

$$= \text{Position}_{\text{canal center}} - \text{Position}_{\text{nail center}} \quad (65)$$

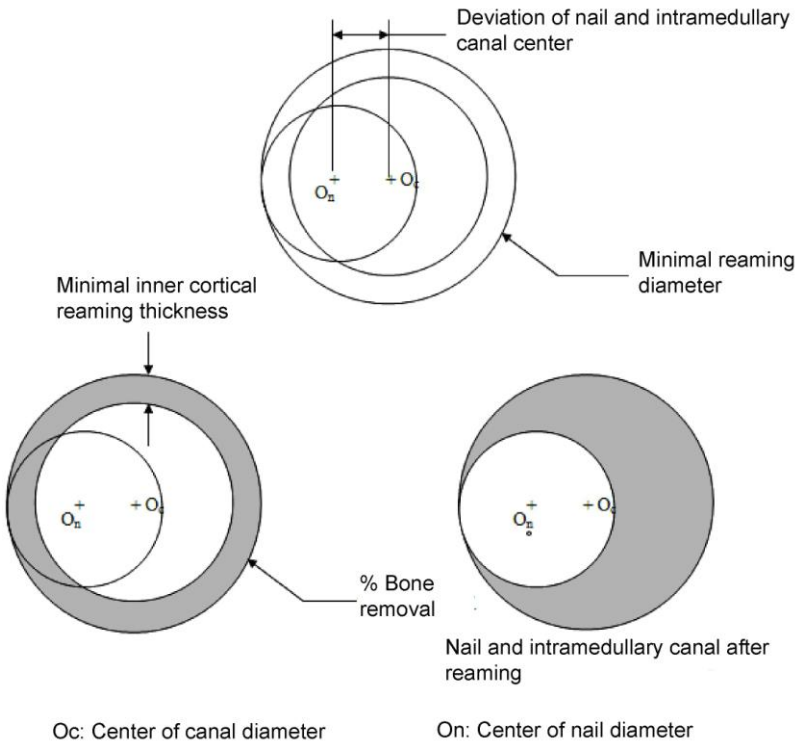

Figure 37 The parameters of fit and fill analysis data shown as the circle of nail and canal for each sections.

2. Finite Element Study of Humeral Nail for Humeral Shaft Fracture

To fully understand the reasons behind the greater biomechanical stability afforded by standard humeral nail, a finite elements study was conducted. Four finite element models were developed in which the humerus geometry and position, bone material properties, nail geometry, nail location, fracture positions, loading and boundary conditions were identical while the humerus position was varied to zero and ninety degree abduction, the gap position was defined as mid-shaft region (Verbruggen *et al*., 2007), nail location was varied to antegrade and retrograde insertion. All finite element models were constructed by MSC PATRAN 2005 and all analyses were performed by MSC MARC/MENTAT 2005 finite element software packages.

2.1 Bone anatomy

The anatomy of the humerus in this series was derived from department of anatomy, faculty of medicine (Siriraj Hospital, Thailand). The inner and outer contour of the bone was classified by different thresholding values from the CT images of this data set. Using CT scanner with 64 slices thickness cross sections were accommodate for entire bone with a spacing of 0.625 mm. The total length of the humerus was 347 mm.

2.2 Fracture Site

The horizontal defects with standard humeral nailing (Russell-Taylor Nail, Smith & Nephew Orthopaedics) was simulated in four independent finite element models. After modeling, a circumferential bone defect of 5 mm was created. The defect position was located at middle of humeral shaft as shown in Figure 38.

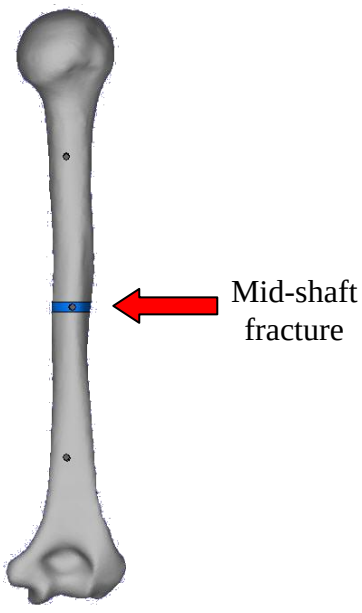

Figure 38 Fractures site of humeral shaft.

2.3 Humeral shaft fracture nailing

A humeral nail (Russell-Taylor nail, 8 mm, Smith & Nephew) stabilized each model humerus. The geometrical characteristics of the nail were derive from 3D laser scan data. According to the manufacturing, a nail length of 220 mm and nail diameter of 8 mm was considered suitable in all humeral shaft fracture sites. One proximal and one distal interlocking bolts were used to stabilize the bony fragments (∅ 4 mm). Stainless steel was selected as the material for nails and bolts.

2.4 Finite element modelling

A three dimensional CAD model of the intact humerus was generated from the mean geometry derived from CT of 76 Thai cadaveric humeri using a Philips spiral CT scanner (64 slices, Tomoscan AV). CT scan acquisition was performed with 0.625 mm slice thickness all of entire bone and reconstruction through CAD software. The humeral nail was inserted virtually into the intramedullary canal of the intact humerus. The proximal screw was inserted through lateral to medial cortex. The distal screw was inserted through anterior to posterior cortex. A 3-dimensional finite element model was generated using four-noded tetrahedral elements based on STL automatic mesh generation technique were used to model of the intact humerus and the humeral nail. In the proximal and distal screw hole on humeral nail were used smaller elements (0.6-mm) to investigate precisely the stress distribution of the implant and the displacement on the bone. The humerus including nail model had a total of 45,606 nodes and 287,680 elements and were presented in Figure 39.

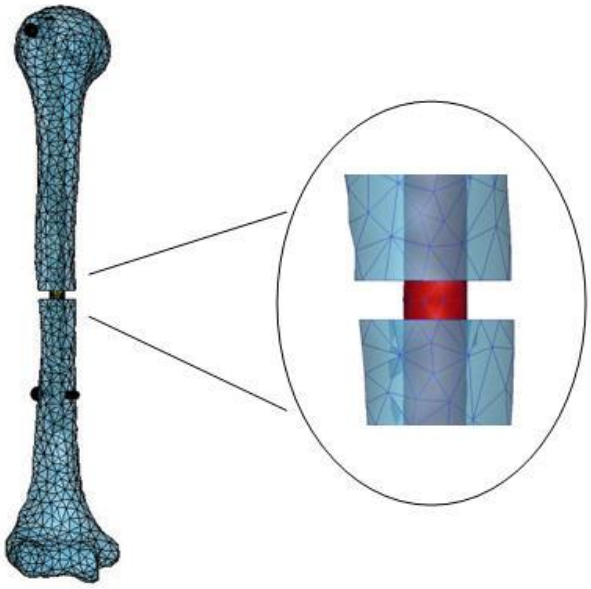

Figure 39 Finite element model. Simulated comminuted fracture and location of elements used for gap closure analysis.

2.5 Material properties

All model in this series were linear elastic isotropic material properties. Different material properties were applied to cortical bone, cancellous bone and fracture gap (or connective tissue) as given in Table 1. For the humeral nail, stainless steel was used for analysis purpose.

Table 1 Material properties of FEA.

Model	Modulus (MPa)	Poisson's ratio
Cortical Bone	14,000	0.3
Cancellous Bone	600	0.2
Connective Tissue	3	0.4
Stainless Steel	200,000	0.3

Source: Duda *et al.* (2001).

2.6 Boundary conditions

The attachments and orientations of 6 muscles that load the shoulder girdle for two different arm positions were derived from the mechanical testing. A single vector represented each muscle. The loading outline for the natural arm position (0°) and 90° abduction were presented in Table 2 and 3, respectively. Four cases studies were observed in this series with different positions/insertion technique and fracture site (Table 4).

2.7 Finite element calculation

The von Mises stress calculation is a universal representation of results in continuum mechanics and applies to ductile materials that fail under shear loading. In contrast to implants that made from metal and since in vivo measurements are limited to strains, equivalent total strains were selected to represent the load status in the bone adequately. All calculations were performed using Marc 2005/ Mentat; Marc Analysis (MTEC, Thailand).

Table 2 Force magnitudes of 6 muscles at neutral position (0° abduction).

Muscle	Force Magnitude (N)	F_X (N)	F_Y (N)	F_Z (N)
Anterior Deltoid	78	-23.09	-10.98	73.69
Lateral Deltoid	25.33	2.07	2.56	25.12
Posterior Deltoid	22	-0.5	-12	18.43
Subscapularis	22	-14.09	-16.17	-4.92
Infraspinatus	58.33	-38.82	-42.49	-9.49
Supraspinatus	206.67	-130.75	-157.47	28.65

Table 3 Force magnitudes of 6 muscles at 90° abduction.

Muscle	Force Magnitude (N)	F_X (N)	F_Y (N)	F_Z (N)
Anterior Deltoid	49.33	-31.33	3.66	37.93
Lateral Deltoid	38	-5.4	-2.28	37.54
Posterior Deltoid	10.67	-7.02	-4.59	6.59
Subscapularis	76.67	-74.56	-7.79	-16.05
Infraspinatus	31.67	-31.09	-2.07	-5.66
Supraspinatus	66	-64.62	-9.2	9.81

Table 4 Four cases study for finite element analysis

Case Study	Lever Arm Position	Approach	Fracture Site
1	Neutral Position (0° Abduction)	Antegrade	Middle Gap
2	Neutral Position (0° Abduction)	Retrograde	Middle Gap
3	90° Abduction	Antegrade	Middle Gap
4	90° Abduction	Retrograde	Middle Gap

RESULTS AND DISCUSSION

1. Geometric Mismatch of Humeral Nail with Antegrade versus Retrograde Insertion in Asian Humerus : A Virtual Simulation Study

1.1 Results

All parameters of geometric mismatch in the case of antegrade and retrograde insertion were shown in table 5 and 6, respectively. The medullary canal diameter averaged 7.85 to 13.78 mm. For antegrade insertion, the minimal reaming diameter needed to enlarge the medullary canal to fit the humeral nail insertion was 8.84 to 14.83 mm, the inner cortical reaming thickness that was needed to be removed before the humeral nail insertion averaged 0.06 to 1.45 mm, the percentage of the removed cortical bone area to fit the humeral nail averaged 3.81 to 107.14 %, and the deviation of the nail center from the canal center averaged 0.42 to 3.42 mm.

For retrograde insertion, the averaged minimal reaming diameter was 8.77 to 29.26 mm, the averaged inner cortical reaming thickness was 0.06 to 9.88 mm, the averaged percentage of the removed cortical bone area was 3.79 to 1287.61% and the averaged deviation of the nail center from the canal center was 0.38 to 10.63 mm.

Figure 40 shows the comparison of minimal reaming diameter between antegrade and retrograde approach, presenting only the minimal reaming diameter values that were significantly different in the same individual. The averaged minimal reaming diameter of antegrade and retrograde in proximal region was 14.83 and 10.06 mm, the averaged minimal reaming diameter of antegrade and retrograde in shaft region was 10.16 and 9.68 mm, and the averaged minimal reaming diameter of antegrade and retrograde in distal region was 10.57 and 29.26 mm.

Table 5 Parameters of geometric mismatch of antegrade insertion technique.

Geometric mismatch parameters	Average (mm)	Standard Deviation(SD)
The diameter of the medullary canal	7.85-13.78	1.29-3.47
The minimal reaming diameter	8.84-14.83	0.60-2.80
The minimal inner cortical reaming thickness	0.06-1.45	0.22-2.00
The percentage of the removed cortical bone area	3.81-107.14 %	15.50-162.60
The deviation of the nail center from center of the medullary canal	0.42-3.42	0.24-1.40

Table 6 Parameters of geometric mismatch of retrograde insertion technique.

Geometric mismatch parameters	Average (mm.)	Standard Deviation(SD)
The diameter of the medullary canal	7.85-13.78	1.29-3.47
The minimal reaming diameter	8.77-29.26	0.44-8.25
The minimal inner cortical reaming thickness	0.06-9.88	0.21-3.22
The percentage of the removed cortical bone area	3.79-1287.61 %	15.15-1400.98
The deviation of the nail center from center of the medullary canal	0.38-10.63	0.22-3.02

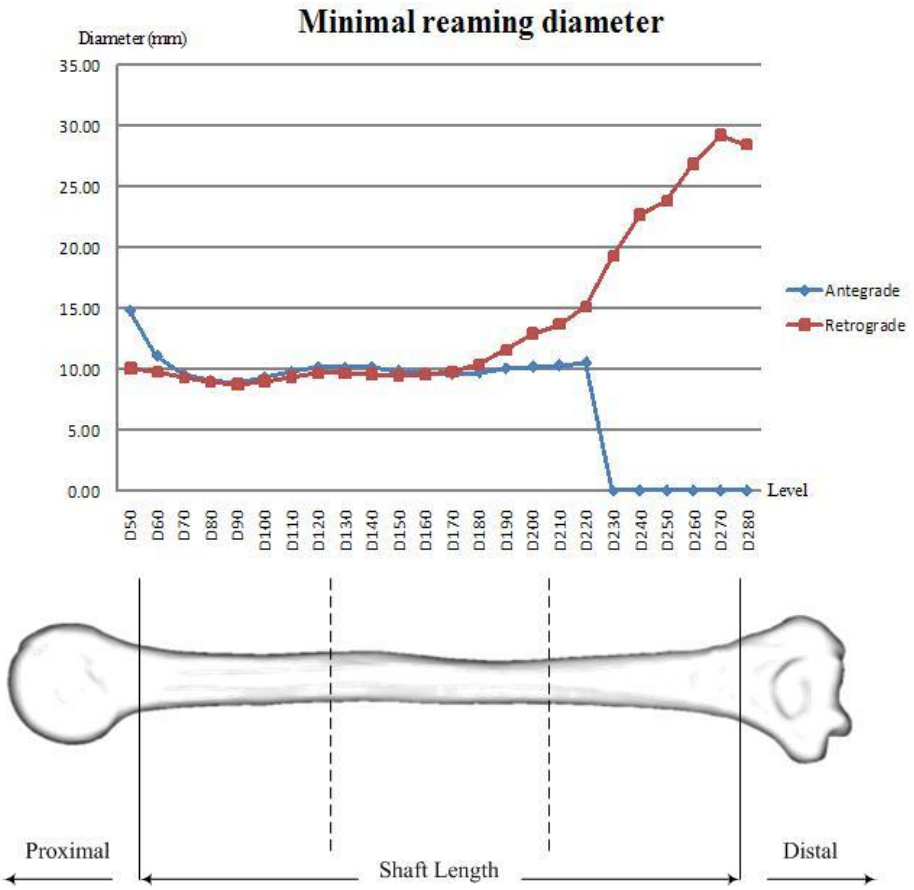

Figure 40 Minimal reaming diameter of antegrade vs retrograde insertion.

1.2 Discussion

The advance of medical imaging technology and computer aided design can assist in simulation analysis to derive the complex structures without destroying the specimens. In this study, measurements of the three dimensional angle and anatomical axis could be easily and precisely performed. The use of medical imaging techniques (computer tomography imaging) combined with three dimensional reverse engineering to evaluate the geometric mismatch would provide better and more precise data than 2-dimensional radiological measurement, consequently improve the design of orthopaedics implant (Leung *et al*., 1996, Chevalley, 2001, and Mahaisavariya *et al*., 2002).

This study focused on the intramedullary nailing in the middle humeral shaft fractures. Previous studies showed that the biomechanical and healing efficiency at this point of antegrade and retrograde insertion did not significantly vary, yet the reaming of medullay canal associated with the risk of re-fracture and bone weakness was not assessed. The antegrade approach is favored for proximal fractures and gives a high rate of healing whereas the retrograde approach is favored for distal fractures (Rommens et al., 1998, Ajmal et al., 2001, Blum et al., 2001, and Cheng and Lin, 2008).

However these are clinical results, the performance of antegrade and retrograde insertion was estimated with healing rate, perioperative problems and healing time. These studies used the Russell-Taylor humeral nail for evaluation because it provides the best biomechanical stability in rotation and is widely used in humeral fracture fixation (Dalton *et al*., 1993).

Previous studies on the geometric mismatch of several designed intramedullary nails in other long bones showed that nails had a mismatch that required over reaming of the cortex volume, thus it would destruct the bone strength and increasing a risk of secondary fracture (Chevalley 2001). These results indicated that the nail format could influence complications in intraoperative or postoperative. However there is no report on the geometric mismatch of the standard humeral nail for the humerus.

This study demonstrated the use of a three-dimensional virtual simulation method to analyze the geometric mismatch of the humeral nail to the humeral canal. The virtual insertion defined optimal entry portal of nailing was referred as actual operative. In other words, the entry point of antegrade insertion was confirmed just medial to the tip of the greater tuberosity (Lin *et al*., 1998, Ajmal *et al*., 2001, Blum *et al*., 2001, Petsatodes *et al*., 2004, Cheng and Lin, 2008, and Muckley *et al*., 2008) and the entry point of retrograde insertion is at the superior edge or higher than the olecranon fossa (Lin *et al*., 1998, Blum *et al*., 2001, Halder *et al*., 2001, Cheng and Lin, 2008, and Muckley *et al*.,2008). Eventually, a complete humeral nailing demands

inserting the nail from the correct entry portal, which reduce the risk of intra-operative fracture (Cheng and Lin, 2008).

From figure 40, the minimal reaming diameter in proximal region (D50-D100) of antegrade approach was larger than the retrograde approach. Contradictory, the minimal reaming diameter in distal region (D180-D280) of antegrade approach was smaller than the retrograde approach. The apparent different values were observed at proximal end of the nail according to insertion techniques. The humeral nail was designed by bending in proximal end, this would be different substantially in reaming diameter values. The average value of medullary canal diameter of the humerus was larger than the nail diameter (8 mm) only in the narrow region and middle shaft region (D130-D200). Therefore, reaming is necessary for insertion of the humeral nail to fit medullary canal. In theory, the minimal reaming diameter is an extreme significant parameter. Over reaming to insert the humeral nail into medullary canal may weaken bone, thereby profuse coincident reaming center will help to reduce the risk of fracture. Significantly, the selection of the humeral nail diameter is important to heal the humeral fractures and decrease the intra operative and post operative complications (Dalton et al., 1993, Rommens et al., 1998, and Cheng and Lin, 2008).

When we considered the minimal reaming diameter at the mid-shaft region of the bone, it was shown that the retrograde technique needed reaming diameter less than antegrade. However, in distal region the retrograde technique produced the critical reaming diameter (D230-D280) due to the technique of retrograde insertion in distal area would have the humeral nail protruded from outer surface of the bone along inclined line of humeral nail. It effected apparent different reaming values. In order to avoid substantial reaming, selection of humeral nail used in surgical operative and nail design should be recommend. In physical consideration, the retrograde technique is better than antegrade technique because the over-reaming of humeral canal would make the shaft weaken and may be bursting in the future. However, but the biomechanical consideration must be proven.

2. Finite Element Study of Humeral Nail for Humeral Shaft Fracture

2.1 Results

2.1.1 Stress distribution

The maximum von Mises stress on the implant such as standard humeral nail, proximal screw, and distal screw illustrated nearly in mid-shaft site (Figure 41 and 42). The intramedullary nail was powerfully sufficient for use to stabilize the humeral shaft fracture in both techniques of antegrade and retrograde insertion.

Table 7 The von Mises stress values of mid-shaft fracture (0° abduction).

Position	Stress distribution (MPa)	
	Antegrade	Retrograde
Proximal screw hole (proximal fragment)	400.36	247.6
Proximal screw	71.52	729.45
Distal screw hole (distal fragment)	574.13	583.51
Distal screw	96.02	196.9

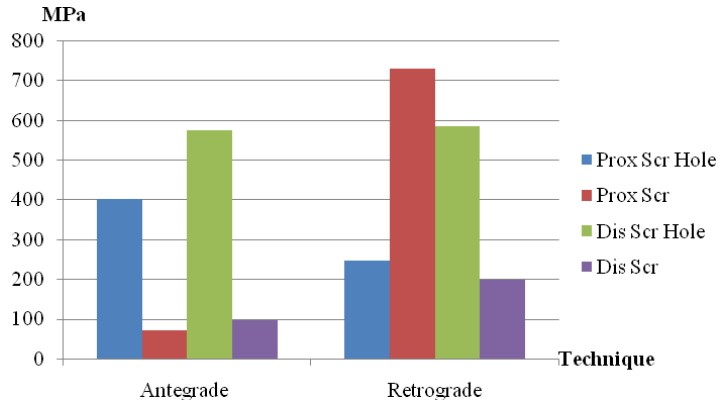

Figure 41 The von Mises stress of mid-shaft fracture at 0° abduction.

Table 8 The von Mises stress values of mid-shaft fracture (90° abduction).

Position	Stress distribution (MPa)	
	Antegrade	Retrograde
Proximal screw hole (proximal fragment)	266.25	173.06
Proximal screw	121.82	235.02
Distal screw hole (distal fragment)	105.82	182.54
Distal screw	55.61	94.81

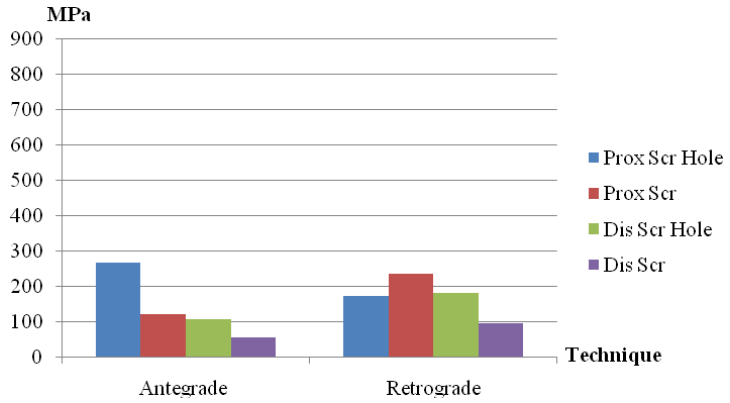

Figure 42 The von Mises stress of mid-shaft fracture at 90° abduction.

2.1.2 Strain distribution

As presented in table 9, the results showed that total strain at 90° abduction was higher than 0° abduction. In case of 0° abduction, the total strain on the bone generated by the retrograde approach was higher strain than that of antegrade approach. The total strain produced by antegrade and retrograde technique was between 14,470-29,430 microstrain, respectively. The 90° abduction is a severe condition for normal abduction. The total strain on the bone generated by retrograde approach was higher than that of antegrade approach, and the total strain of antegrade and retrograde techniques occured between the 49,650-58,090 microstrain, respectively.

Table 9 The total strain on bone surface.

Technique	Equivalent total strain on bone (με)	
	0° Abduction	90° Abduction
Antegrade	14,470	49,650
Retrograde	29,430	58,090

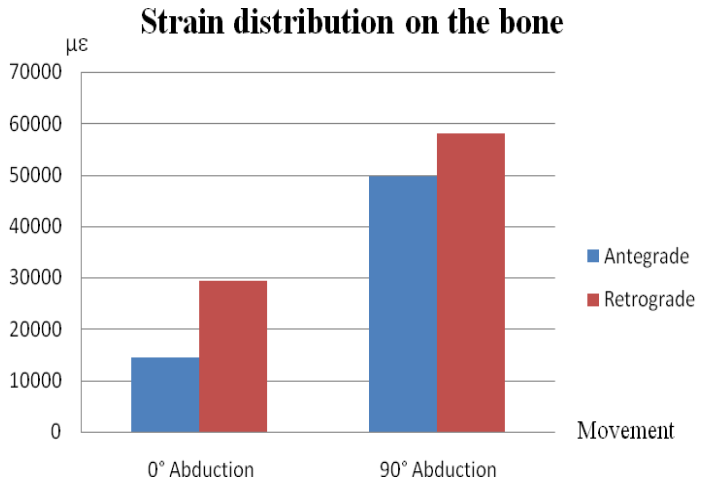

Figure 43 Strain distribution on the bone.

2.2 Discussion

Knowledge regarding stress distribution on the implant and bone straining are important for understanding implant failure and origin of fractures. The aim of this study is to investigate the influence of intramedullary nail fixation with standard humeral nail and muscle forces generated by movement of the arm on the straining of bone in mid-shaft fracture sites. A 5 mm bone defect configuration was used to eliminate the influence of the contact variable between the bone segments and implant (Lin *et al.*, 1998). Due to the stress and strain distribution of the composite structure is not actually linear, finite element method is the best selection to evaluate or predict the mechanical behavior of orthopaedics implants. Generally, humeri that can be nailed from either the proximal or the distal end are a good model for biomechanical

comparison between different nailing directions. However, there are several designs of humeral nail for the fixation of humeral shaft fractures, which are made of stainless steel, such as the Russell-Taylor nail. The RT humeral nail has been widely used in the Asia-Pacific region. The current study used the RT humeral nail measures only 8 mm in distal diameter, with one distal locking screw hole, whereas the proximal diameter is 9 mm to accept the 4 mm proximal screw.

2.2.1 Stress distribution

From the results (Figure 44-47), it was showed that stress distribution on implant extended highly from both screw holes. At 0° abduction, the retrograde approach produced the stress distribution value higher than antegrade approach, which rose almost in all positions. At the arm position of 90° abduction, the retrograde approach produced the stresses significantly higher than antegrade approach. These results suggested that generated stress were concentrated in both screw hole of intramedullary nail, then the stresses extended along nail surface or adjacent area. Moreover, amount of contact area between medullary canal and nail affected stress concentration. We speculate that pulled down load from arm weight and muscle forces were transferred to the bone, it will produce the strain on proximal and distal bone more than other region. The strain affected proximal and distal screw, subsequently the bending load was transmitted to both screw hole of the implant. Nevertheless, the retrograde nailing produced higher stress than antegrade nailing. This augmentation affected the bone where the stress distribution on bone surface was observe (Figure 46-47). Furthermore, the nail could weaken the bone strength of the humeral shaft adjacent to the nail due to the stress shielding phenomena (Sitthiseripratip *et al*., 2003).

After fracture healing, the humeral nail itself may fail in the long period since high stress levels are still transferred through and located in the nail. Therefore it is suitable to remove the humeral nail after the fracture healing to minimize the problem of failure of the implant, possibly by cyclic fatigue failure (Sitthiseripratip *et al*., 2003).

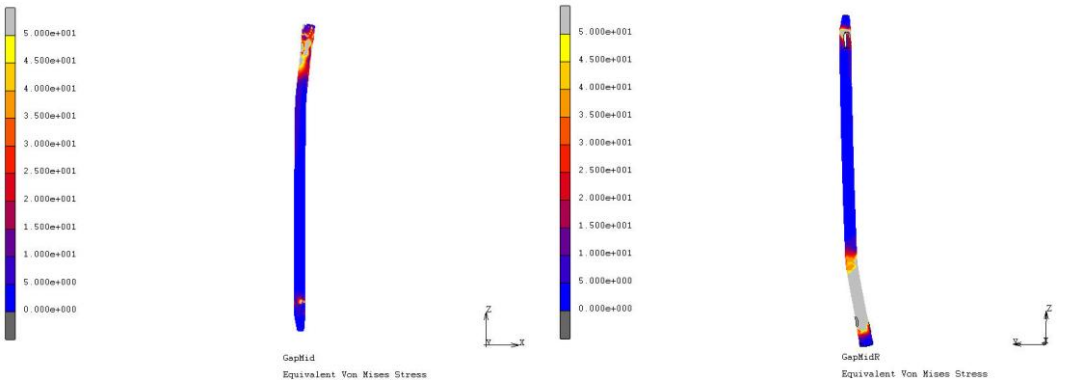

(A) (B)

Figure 44 The von Mises stress on standard humeral nail at 0° abduction: (A) Antegrade insertion and (B) Retrograde insertion.

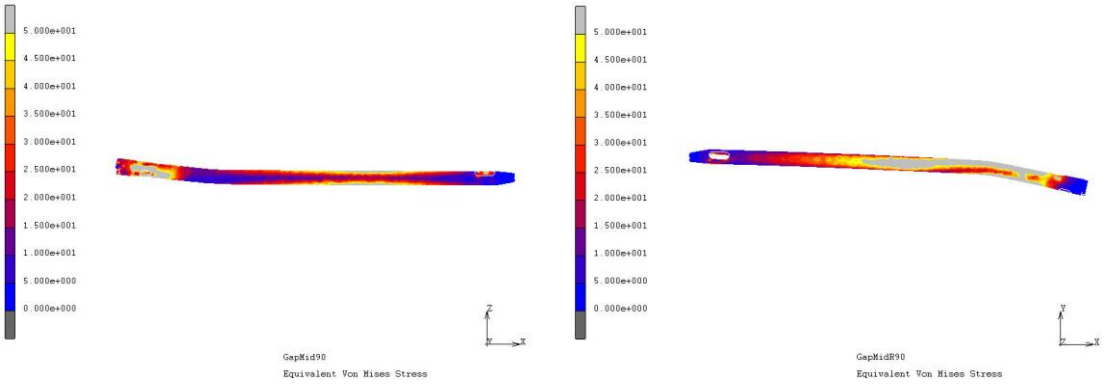

(A) (B)

Figure 45 The von Mises stress on standard humeral nail at 90° abduction: (A) Antegrade insertion and (B) Retrograde insertion.

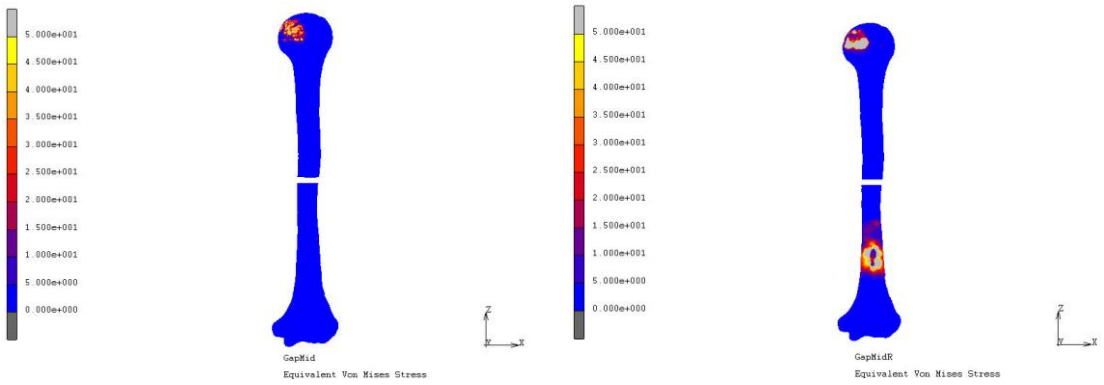

(A) (B)

Figure 46 The von Mises stress on the bone at 0° abduction: (A) Antegrade insertion and (B) Retrograde insertion.

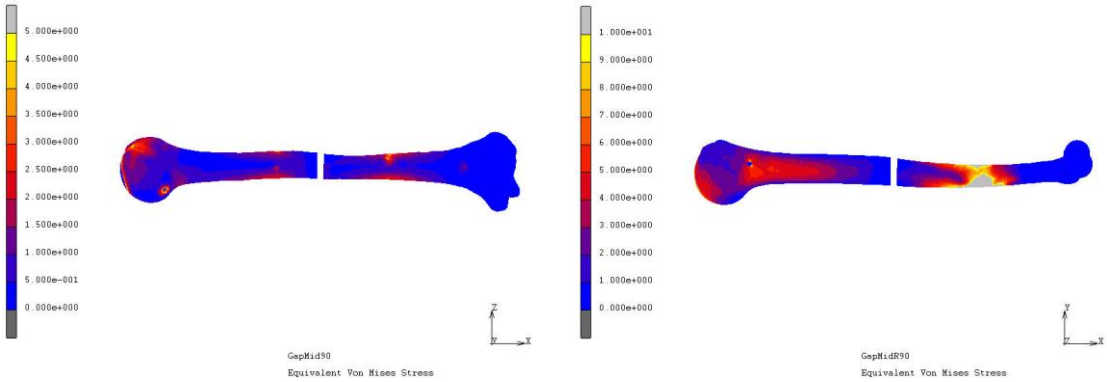

(A) (B)

Figure 47 The von Mises stress on the bone at 90° abduction: (A) Antegrade insertion and (B) Retrograde insertion.

2.2.2 Strain distribution

From table 9, the maximum strain value on mid-shaft fracture gap of 0° abduction were generated by retrograde nailing as well as the 90° abduction (Figure 48 and 49). The previous study reported that under physiological-like musculo-skeletal loading maximum strains were found for 90° abduction (Maldonado *et al*., 2003). However, all case study showed that the maximum strain values had fallen into the pathological overload zone (Figure 50). This will risk occurence of non-union or re-fracture of bone fragments due to extreme strain distribution over the

pathological-over load zone. Therefore the patient in case of humeral shaft fracture did not carry the heavy load and elevate the arm in 90° abduction.

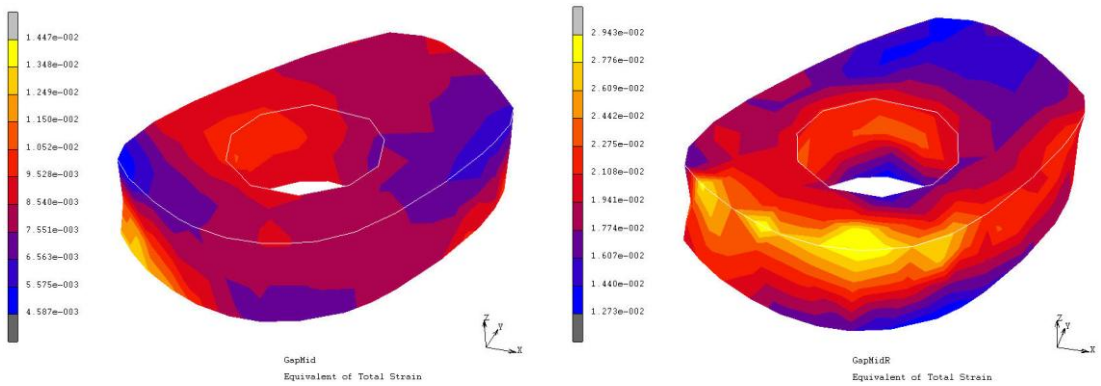

(A) (B)

Figure 48 The strain distribution on the fracture gap at 0° abduction: (A) Antegrade insertion and (B) Retrograde insertion.

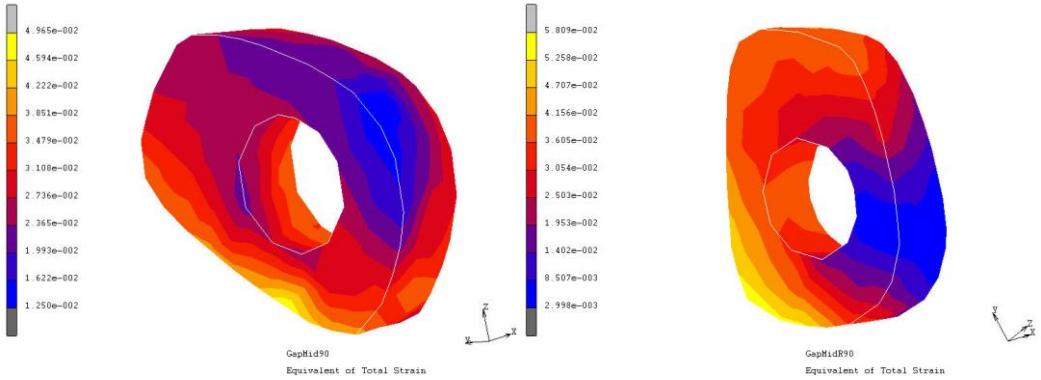

(A) (B)

Figure 49 The strain distribution on the fracture gap at 90° abduction: (A) Antegrade insertion and (B) Retrograde insertion.

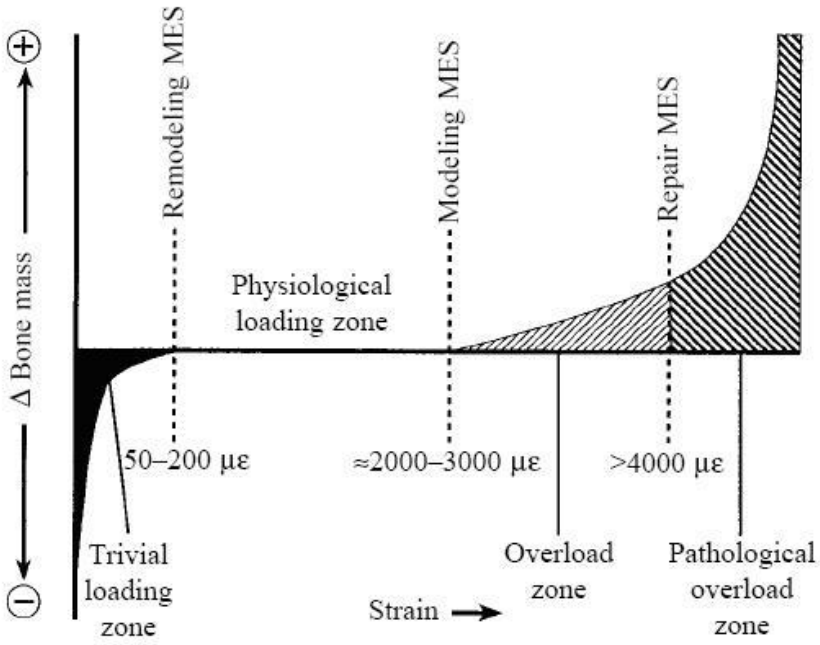

Figure 50 Graph of Frost's mechanostat theory show the behavior of strain distribution on bone.

Source: Su *et al*. (1999).

CONCLUSION AND RECOMMENDATION

1. Conclusions

1.1 Geometric mismatch of humeral nail with antegrade versus retrograde insertion in asian humerus

Some studies evaluated the mismatch of nail and bone by 2-dimensional (Leung *et al*., 1996, Chavalley, 2001, and Akpinar *et al*., 2003) and 3-dimensional data (Mahaisavariya *et al.*, 2004). This study demonstrated some mismatching of three-dimensional geometry of standard humeral nail to Asian humerus. Proper reaming to prepare the medullary canal should be considered to accommodate the nail insertion and to prevent clinical complications. Re-design of the implant may be taken into account for better treatment in the Asian patients.

1.2 Finite element study of humeral nail for humeral shaft fracture

In this study, the muscle forces of rotator cuff and deltoid produced the initial load to the humerus when hanging the arm. It differed from the femur and tibia that the body weight was the main effect for generating the initial load on the proximal bone. The finite element study presented that the retrograde approach gave a good result in biomechanical stability. Therefore the retrograde technique was preferred than antegrade technique. For the post operative of humeral shaft fracture, the patient should hang the arm in zero degree abduction or natural position and avoid the ninety degree abduction.

2. Recommendation for further research

In the future, humeral nail re-designing was recommended to suite Thai patients. In addition, finite element study of various intramedullary nail design with humeral shaft fractures should be perform to determine available physiological like loading conditions and best humeral nail for patients.

LITERATURE CITED

Ajmal, M., M. O'Sullivan, J. McCabe and W. Curtin. 2001. Antegrade locked intramedullary nailing in humeral shaft fractures. **Injury** 32(9): 692-4.

Akpinar, F., A. Aydinlioglu, N. Tosun, A. Dogan, I. Tuncay and O. Unal. 2003. A morphometric study on the humerus for intramedullary fixation. **Tohoku J Exp Med** 199(1): 35-42.

Arunjarutthum, P., K. Sitthiseripratip, B. Mahaisavariya, P. Saiviroonporn and T. Kiatwat. 2006. Morphometric Study of the Thai Humerus : A Cadaveric Study, 153-154. **ISBME 2006**. Bangkok, Thailand.

Bathe, K. J. (1996). **Finite Element Procedures.** New Jersey, Prentice-Hall.

Bishop, R.C., K.A. Moore and M.N. Hadley. 1996. Anterior cervical interbody fusion using autogeneic and allogeneic bone graft substrate: a prospective comparative analysis. **J. Neurosurg**: 206–210.

Blum, J., H. Janzing, R. Gahr, H.S. Langendorff and P.M. Rommens. 2001. Clinical performance of a new medullary humeral nail: Antegrade versus retrograde insertion. **J. Ortho Trauma**: 342-349.

Blumenthal, S.L., J. Baker and A. Dossett. 1988. The role of anterior lumbar fusion for internal disc disruption. **Spine**: 566–569.

Boileau, P. and G. Walch. 1997. The three-dimensional geometry of the proximal humerus. **J. Bone Joint Surg**: 857-865.

Brown, C.W., T.J. Orme and H.D. Richardson. 1986. The rate of pseudarthrosis (surgical nonunion) in patients who are smokers and patients who are nonsmokers: a comparison study. **Spine**: 942–943.

Browner, B.D., J.B. Jupiter, A.M. Levine and P.G. Trafton. 1998. **Skeleton Trauma: Fractures, Dislocations, Ligamentous Injuries.** 2nd ed. W.B. Saunders Company, United State of America.

Burchardt, H. and W.F. Enneking. 1978. Transplantation of bone. **Surg Clin North Am**: 403–427.

Cheng, H. R. and J. Lin. 2008. Prospective randomized comparative study of antegrade and retrograde locked nailing for middle humeral shaft fracture. **J Trauma** 65(1): 94-102.

Cross, A. R. and D. D. Lewis. **Fracture management, bone healing and grafting.** University of Florida., College of Veterinary Medicine.

Daftari, T.K., T.E. Jr Whitesides and J.G. Heller. 1994. Nicotine on the revascularization of bone graft. An experimental study in rabbits. **Spine**: 904–911.

Dalton, J. E., S. L. Salkeld, Y.E. Satterwhite and S.D. Cook. 1993. A biomechanical comparison of intramedullary nailing systems for the humerus. **J Orthop Trauma** 7(4): 367-74.

Debski, R.E., P.J. McMahon, W.O. Thompson, S.L-Y. Woo, J.J.P. Warner and F.H. Fu. 1995. A new dynamic testing apparatus to study glenohumeral joint motion. **J. Biomechanics**: 869-874.

DePalma, A.F., R.H. Rothman and G.E. Lewinnek. 1972. Anterior interbody fusion for severe cervical disc degeneration. **Surg Gynecol Obstet**: 755–758.

Duda, N.G., F. Mandruzzato, M. Heller, J. Goldhahn, R. Moser, M. Hehli, L. Claes and P.N. Hass. 2001. Mechanical boundary conditions of fracture healing: borderline indications in the treatment of undreamed tibial nailing. **J. Biomech**: 639-650.

Francois Chevalley, P. R. 2001. Fit-and-Fill Analysis of Different Intramedullary Nails for the Proximal Femur. **European Journal of Trauma** 4: 178-183.

Halder, S. C., J. A. Chapman, G. Choudhury and W.A. Wallace. 2001. Retrograde fixation of fractures of the neck and shaft of the humerus with the 'Halder humeral nail'. **Injury** 32(9): 695-703.

Kalfas, I.H. 2001. Principles of bone healing. **Neurosurg Focus**: 1-4.

Kedgley, A.E., G.A. Mackenzie, L.M. Ferreira, D.S. Drosdowech, G.J.W. King, K.J. Faber and J.A. Johnson. 2007. The effect of muscle loading on the kinematics of in vitro glenohumeral abduction. **J. Biomechanics**: 1-8.

Leung, K.S., P. Procter, B. Robioneck and K. Behrens. 1996. Geometric mismatch of the gamma nail to the Chinese femur. **Clinical Orthopaedics and Related Research**: 42-48.

Lin, J., N. Inoue, A. Valdevit, Y.S. Hang, S.M. Hou and E.Y.S. Chao. 1997. Biomechanical comparison of antegrade and retrograde nailing of humeral shaft fracture. **J. Clinorthop**: 203-213.

Mahaisavariya, B., K. Sitthiseripratip, T. Tongdee, L.J.E. Bohez, V.J. Sloten and P. Olis. 2002. Morphological study of the proximal femur: a new method of geometrical assessment using 3-dimensional reverse engineering. **J. Medical Engineering & Physics**: 617-622.

Mahaisavariya, B., K. Sitthiseripratip, P. Oris, E. Chaichanasiri and J. Suwanprateeb. 2004. Fit-and-fill analysis of trochanteric gamma nail for the thai proximal femur: A virtual simulation study. **J. Med Assoc Thai**: 1315-1320.

Maldonado, Z.M., J. Seebeck, M.O.W. Heller, D. Brandt, P. Hepp, H. Lill and G.N. Duda. 2003. Straining of the intact and fractured proximal humerus under physiological-like loading. **J. Biomech**: 1865-1873.

Moaveni, S. 1999. **Finite Element Analysis Theory and Application with ANSYS.** Prentice-Hall, Inc., New Jersey.

Muckley, T., M. Diefenbeck, A. Sorkin, C. Beimel, M. Goebel and V. Buhren. 2008. Results of the T2 humeral nailing system with special focus on compression interlocking. **Injury** 39(3): 299-305.

Neer, C. S., 2nd 2006. Displaced proximal humeral fractures: part I. Classification and evaluation. 1970. **Clin Orthop Relat Res** 442: 77-82.

Petsatodes, G., D. Karataglis, P. Papadopoulos, J. Christoforides, John Gigis and John Pournaras. 2004. Antegrade interlocking nailing of humeral shaft fractures. **J Orthop Sci** 9(3): 247-52.

Recker, R.R. 1992. Embryology, anatomy, and microstructure of bone, in Coe FL, Favus MJ (eds): Disorders of Bone and Mineral Metabolism. New York, Raven: 219–240.

Riebel, E.D., S.D. Boden and T.E. Whitesides. 1995. The effect of nicotine on incorporation of cancellous bone graft in an animal model. **Spine**: 2198–2202.

Rommens, P. M. and J. Blum. 1998. Retrograde nailing of humeral shaft fractures. **Clin Orthop Relat Res** (350): 26-39.

Rubenstein, I., T. Yong and S.I. Rennard. 1991. Cigarette smoke extract attenuates endothelium-dependent arteriolar dilation in vivo. **Am J Physiol**: H1913–H1918.

Silcox, D.H. III, T. Daftari and S.D. Boden. 1995. The effects of nicotine on spinal fusion. **Spine**: 1549–1553.

Sitthiseripratip, K., H. van Oosterwyck, J.V. Sloten, B. Mahaisavariya, E.L.J. Bohez, J. Suwanprateeb, R. van Audekercke and P. Oris. 2002. Finite element study of trochanteric gamma nail for trochanteric fracture. **J. Med Eng Phy**: 99-106.

Su, C.S., G.J. Skedros, N.K. Bachus and D.R. Bloebaum. 1999. Loading conditions and cortical bone construction of an artiodactyls calcaneus. **J. Exp Bio**: 3239-3254.

Van der Helm, F.C.T. and R. Veenbaas. 1991. Modelling the mechanical effect of muscles with large attachment sites: Application to the shoulder mechanism. **J. Biomechanics**: 1151-1163.

Wolff, J. 1986. The Law of Bone Remodelling. Translated by Maquet P. Furlong R. Berlin: Springer-Verlag.

Wuelker, N., C.J. Wirth, W. Plitz and B. Roetman. 1993. A dynamic shoulder model: Reliability testing and muscle force study. **J. Biomechanics**: 489-499.

APPENDIX

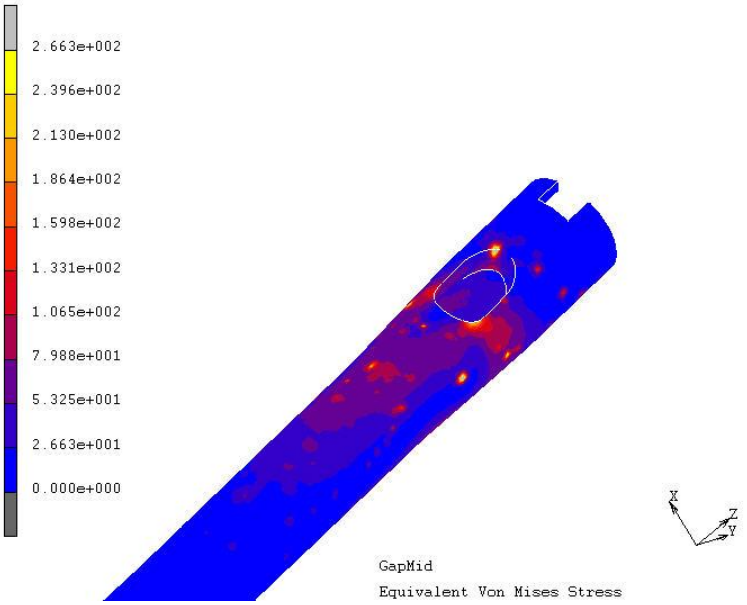

Appendix Figure 1 The von Mises stress on proximal screw hole at middle gap in 0° abduction of antegrade insertion.

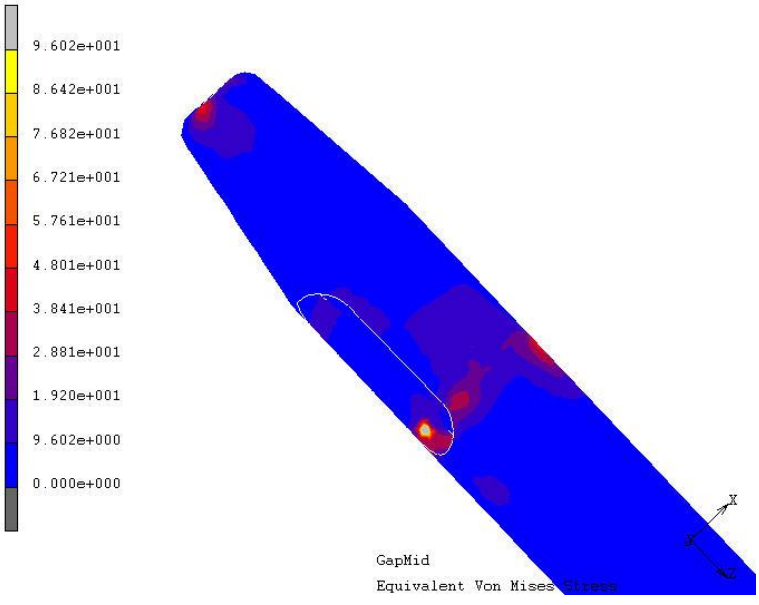

Appendix Figure 2 The von Mises stress on distal screw hole at middle gap in 0° abduction of antegrade insertion.

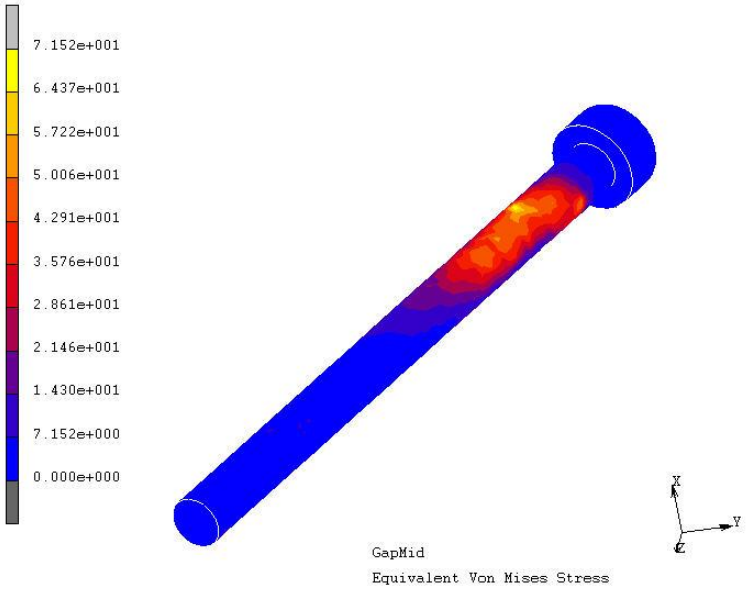

Appendix Figure 3 The von Mises stress on proximal screw at middle gap in 0° abduction of antegrade insertion.

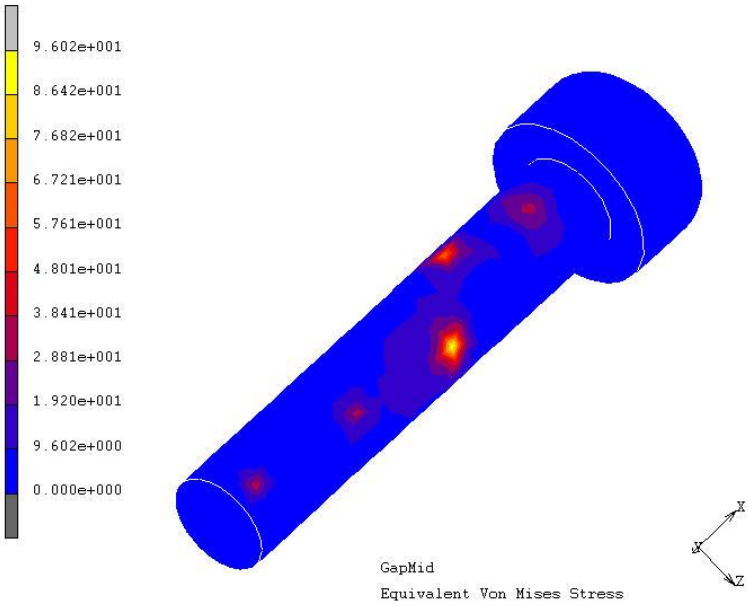

Appendix Figure 4 The von Mises stress on distal screw at middle gap in 0° abduction of antegrade insertion.

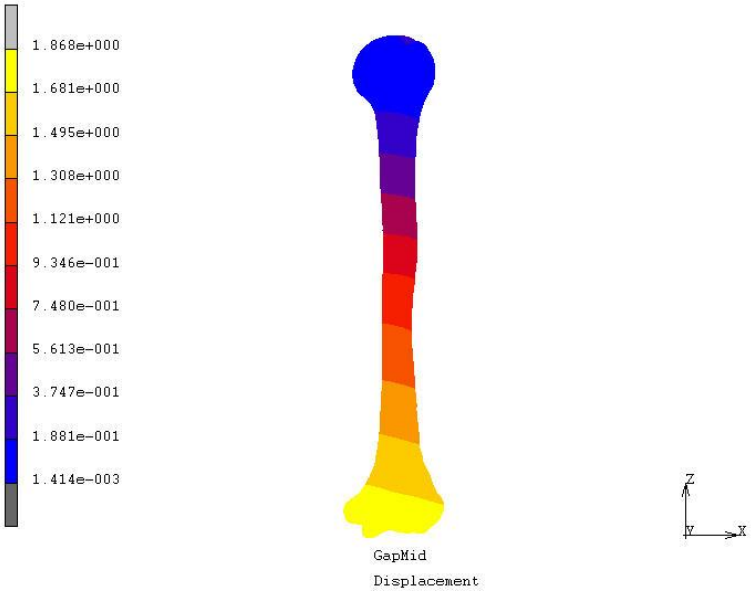

Appendix Figure 5 The displacement on the bone at middle gap in 0° abduction of antegrade insertion.

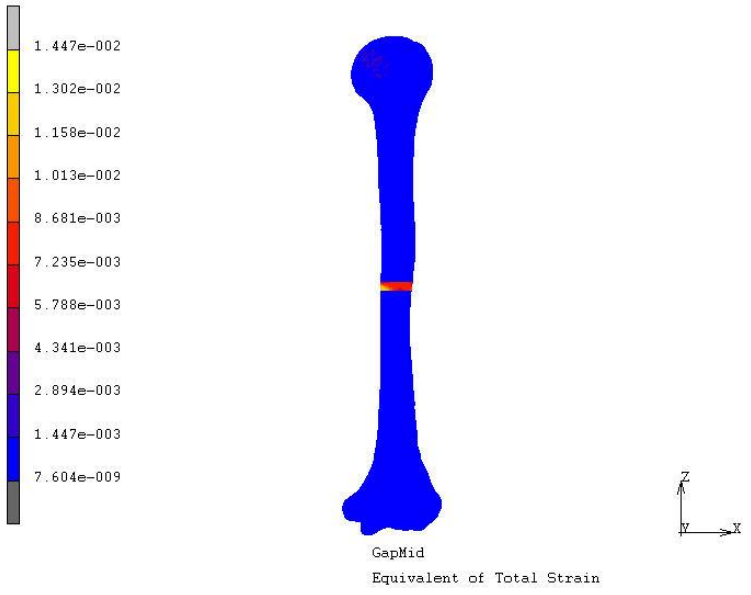

Appendix Figure 6 The total strain on the bone at middle gap in 0° abduction of antegrade insertion.

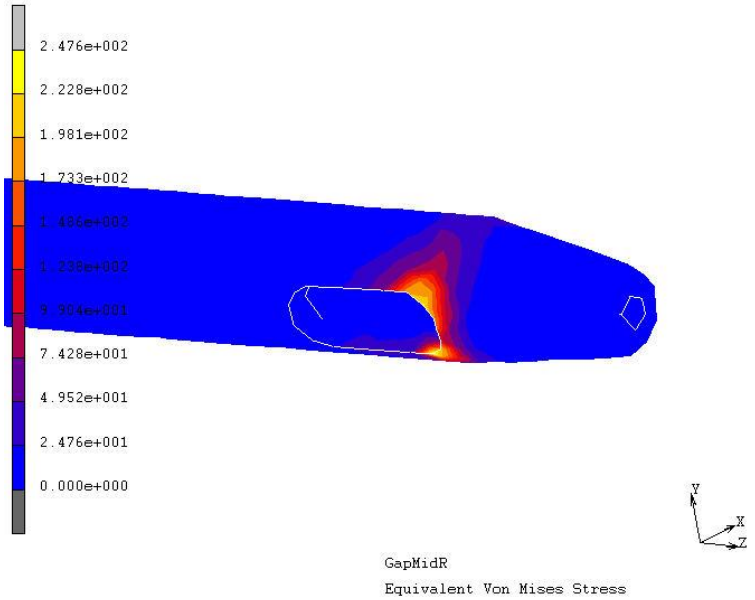

Appendix Figure 7 The von Mises stress on proximal screw hole at middle gap in 0° abduction of retrograde insertion.

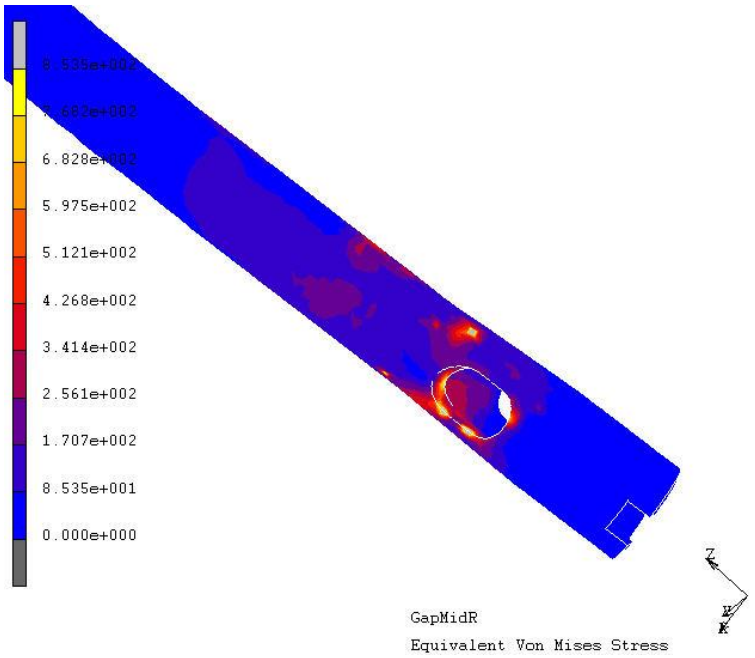

Appendix Figure 8 The von Mises stress on distal screw hole at middle gap in 0° abduction of retrograde insertion.

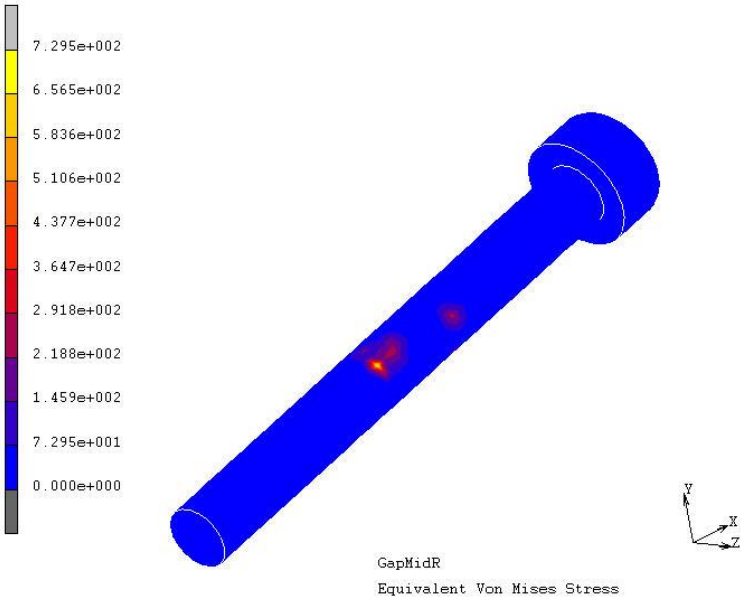

Appendix Figure 9 The von Mises stress on proximal screw at middle gap in 0° abduction of retrograde insertion.

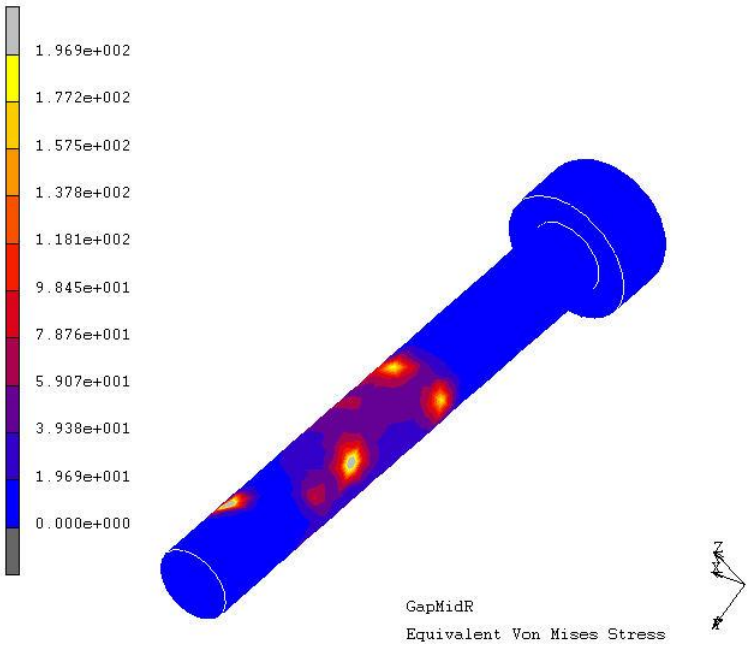

Appendix Figure 10 The von Mises stress on distal screw at middle gap in 0° abduction of retrograde insertion.

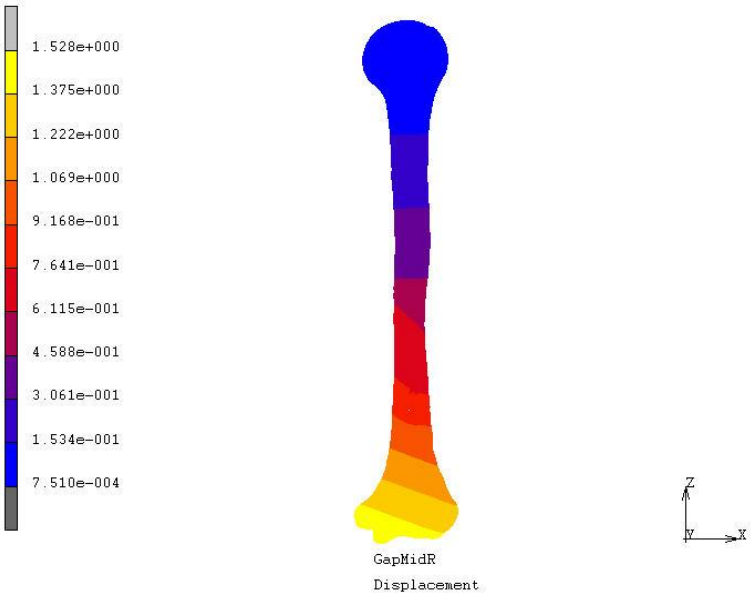

Appendix Figure 11 The displacement on the bone at middle gap in 0° abduction of retrograde insertion.

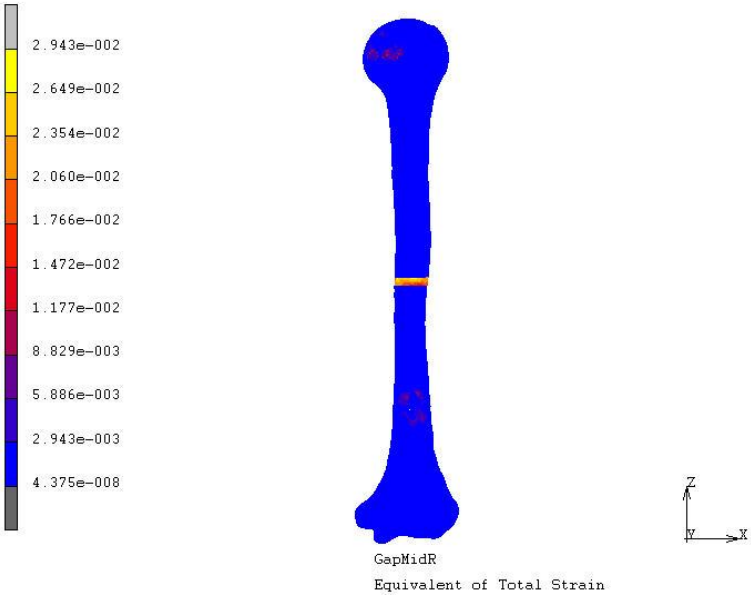

Appendix Figure 12 The total strain on the bone at middle gap in 0° abduction of retrograde insertion.

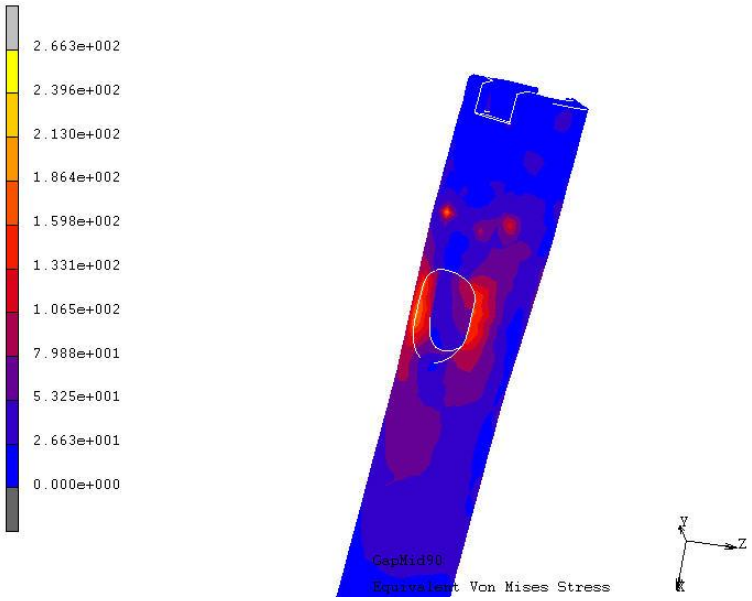

Appendix Figure 13 The von Mises stress on proximal screw hole at middle gap in 90° abduction of antegrade insertion.

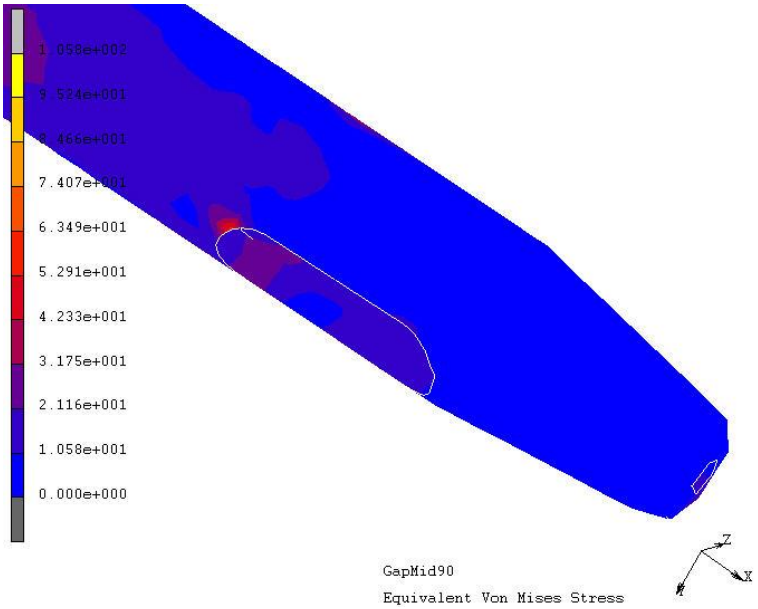

Appendix Figure 14 The von Mises stress on distal screw hole at middle gap in 90° abduction of antegrade insertion.

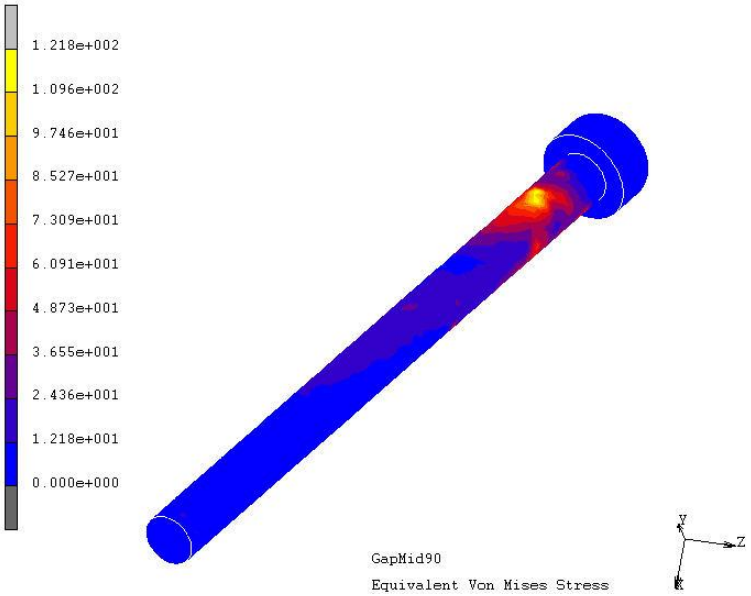

Appendix Figure 15 The von Mises stress on proximal screw at middle gap in 90° abduction of antegrade insertion.

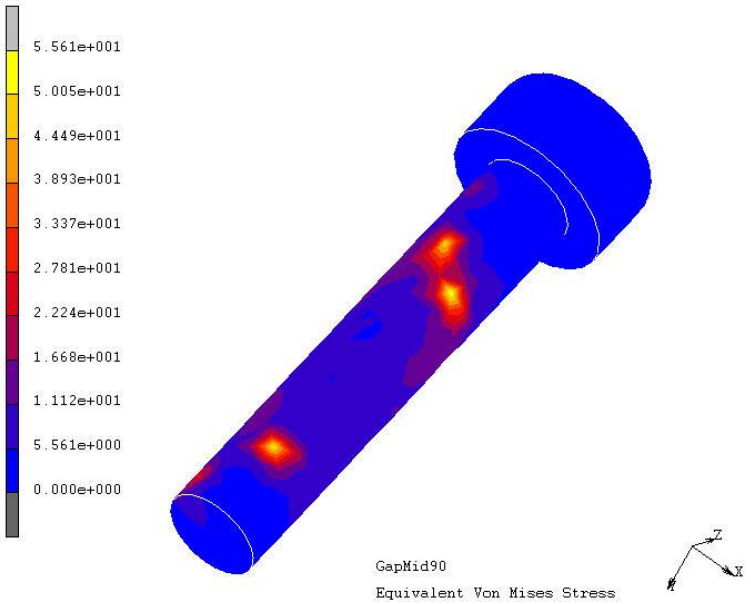

Appendix Figure 16 The von Mises stress on distal screw at middle gap in 90° abduction of antegrade insertion.

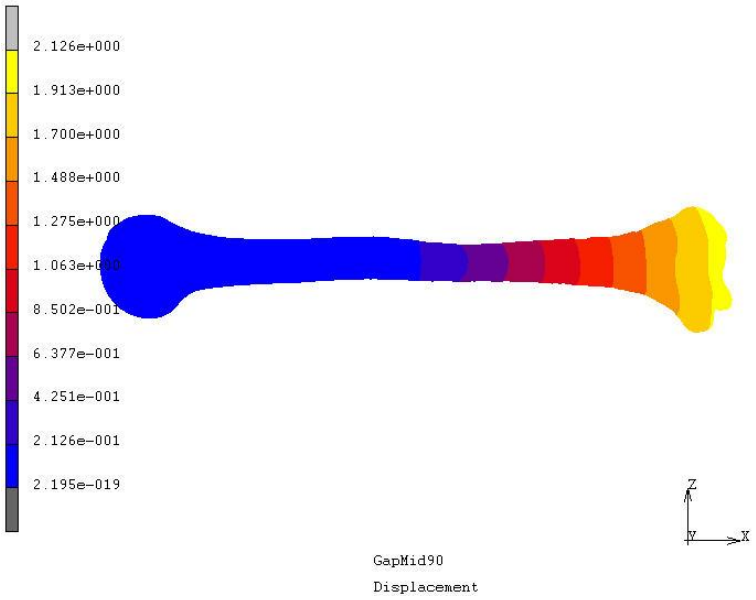

Appendix Figure 17 The displacement on the bone at middle gap in 90° abduction of antegrade insertion.

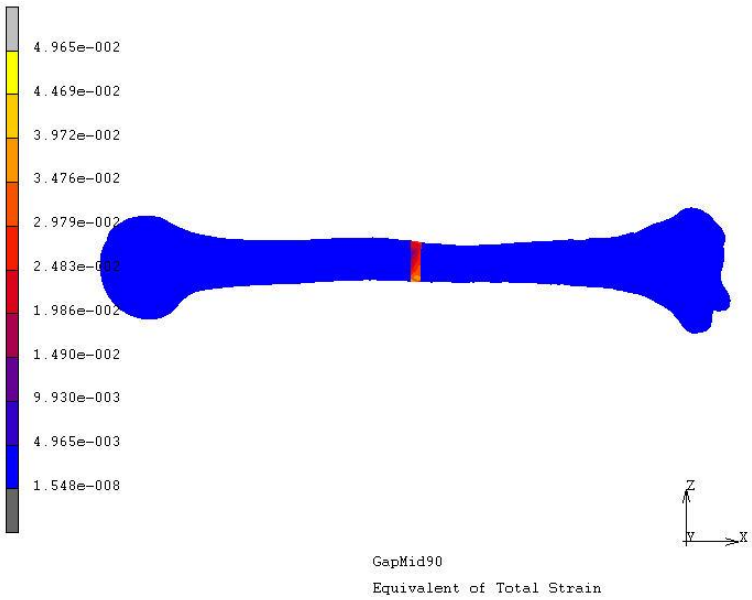

Appendix Figure 18 The total strain on the bone at middle gap in 90° abduction of antegrade insertion.

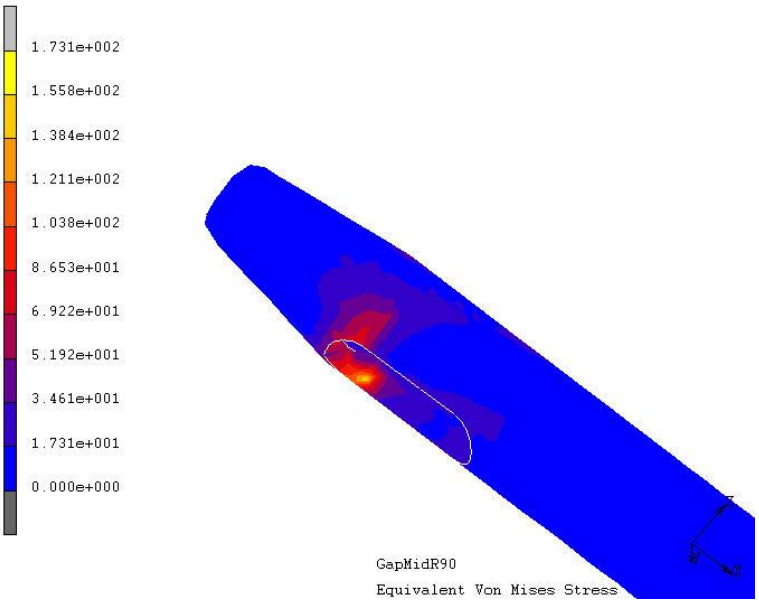

Appendix Figure 19 The von Mises stress on proximal screw hole at middle gap in 90° abduction of retrograde insertion.

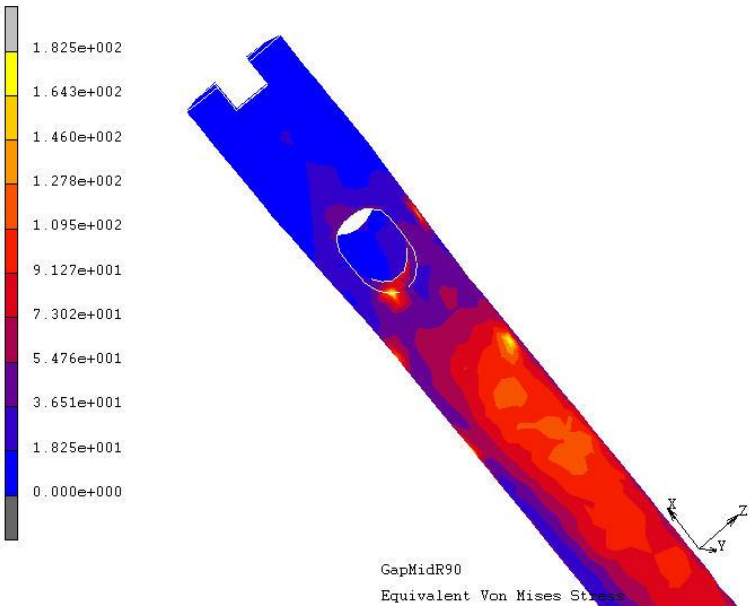

Appendix Figure 20 The von Mises stress on distal screw hole at middle gap in 90° abduction of retrograde insertion.

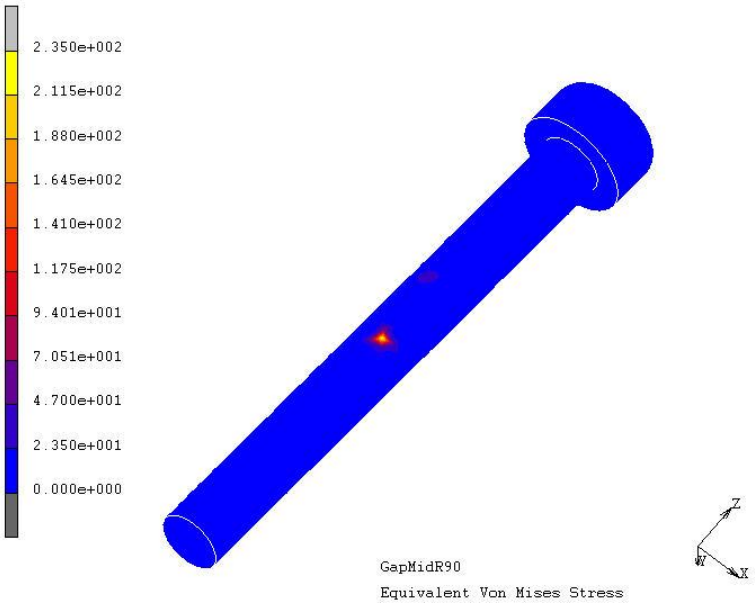

Appendix Figure 21 The von Mises stress on proximal screw at middle gap in 90° abduction of retrograde insertion.

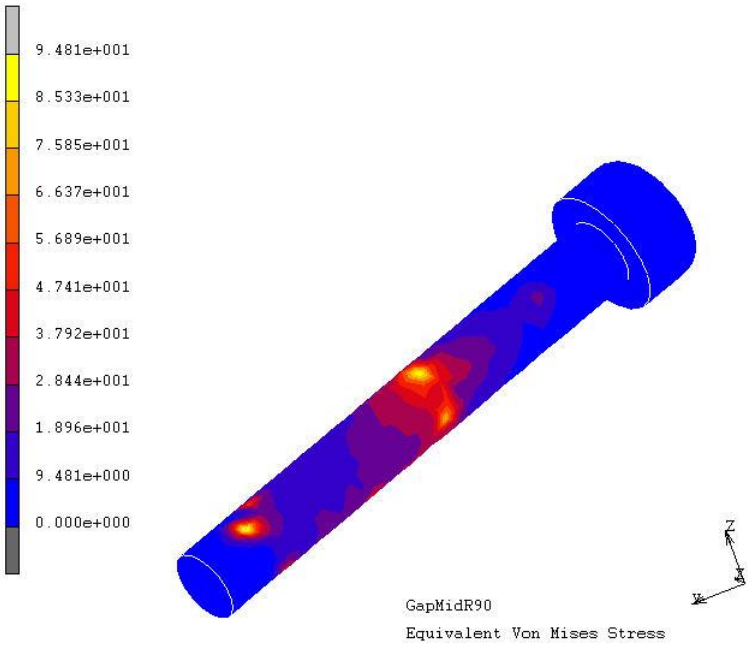

Appendix Figure 22 The von Mises stress on distal screw at middle gap in 90° abduction of retrograde insertion.

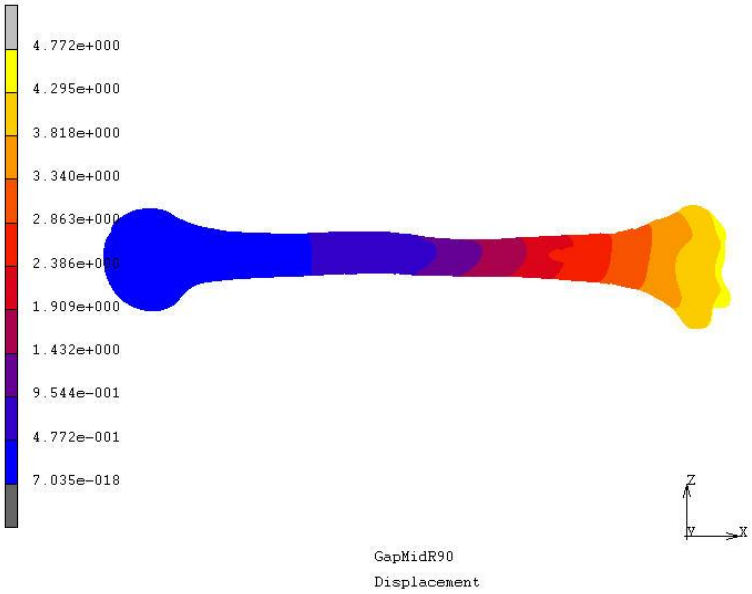

Appendix Figure 23 The displacement on the bone at middle gap in 90° abduction of retrograde insertion.

Appendix Figure 24 The total strain on the bone at middle gap in 90° abduction of retrograde insertion.

CIRRICULUM VITAE

NAME	Mr. Pongnarin Jeamwatthanachai
BIRTH DATE	December 15, 1982
BIRTH PLACE	Bangkok, Thailand
EDUCATION	Year Institute Degree
	2005 Rajamangala Univ. B.Eng (Food Eng.)
POSITION/TITLE	Student
WORKPLACE	Medical Rapid Prototyping Laboratory, MTEC
SCHOLARSHIP	Thai Graduate Institute of Science and Technology